

# Intertwined eco-morphodynamic evolution of salt marshes and tidal channels cutting through them

Geng, Liang; D'Alpaos, Andrea; Sgarabotto, Alessandro; Gong, Zheng; Lanzoni, Stefano

DOI:

[10.1002/essoar.10507617.1](https://doi.org/10.1002/essoar.10507617.1)

License:

Creative Commons: Attribution-NonCommercial (CC BY-NC)

*Document Version*

Publisher's PDF, also known as Version of record

*Citation for published version (Harvard):*

Geng, L, D'Alpaos, A, Sgarabotto, A, Gong, Z & Lanzoni, S 2021 'Intertwined eco-morphodynamic evolution of salt marshes and tidal channels cutting through them' ESS Open Archive.  
<https://doi.org/10.1002/essoar.10507617.1>

[Link to publication on Research at Birmingham portal](#)

## General rights

Unless a licence is specified above, all rights (including copyright and moral rights) in this document are retained by the authors and/or the copyright holders. The express permission of the copyright holder must be obtained for any use of this material other than for purposes permitted by law.

- Users may freely distribute the URL that is used to identify this publication.
- Users may download and/or print one copy of the publication from the University of Birmingham research portal for the purpose of private study or non-commercial research.
- User may use extracts from the document in line with the concept of 'fair dealing' under the Copyright, Designs and Patents Act 1988 (?)
- Users may not further distribute the material nor use it for the purposes of commercial gain.

Where a licence is displayed above, please note the terms and conditions of the licence govern your use of this document.

When citing, please reference the published version.

## Take down policy

While the University of Birmingham exercises care and attention in making items available there are rare occasions when an item has been uploaded in error or has been deemed to be commercially or otherwise sensitive.

If you believe that this is the case for this document, please contact [UBIRA@lists.bham.ac.uk](mailto:UBIRA@lists.bham.ac.uk) providing details and we will remove access to the work immediately and investigate.

1 **Intertwined eco-morphodynamic evolution of salt**  
2 **marshes and tidal channels cutting through them**

3 **Liang Geng<sup>1,2</sup>, Andrea D’Alpaos<sup>3</sup>, Alessandro Sgarabotto<sup>2</sup>, Zheng Gong<sup>1</sup>, and**  
4 **Stefano Lanzoni<sup>2</sup>**

5 <sup>1</sup>State Key Laboratory of Hydrology Water Resources and Hydraulic Engineering, Hohai University,  
6 Nanjing, China

7 <sup>2</sup>Department of Civil, Environmental and Architectural Engineering, University of Padova

8 <sup>3</sup>Department of Geosciences, University of Padova

9 **Key Points:**

- 10 • Vegetation with lower optimal elevation strongly promotes the development, com-  
11 plexity and drainage efficiency of channel networks.
- 12 • Vegetation patches affect the distribution of sediment deposition by trapping sed-  
13 iment and reducing the landward sediment transport.
- 14 • Sea level rise restricts the extension of salt marshes and consequently leads to re-  
15 duced control of vegetation on tidal channel development.

---

Corresponding author: Liang Geng, [liang.geng@dicea.unipd.it](mailto:liang.geng@dicea.unipd.it)

## 16 Abstract

17 The formation and development of tidal channels and salt marshes are controlled  
18 by complex interactions between hydrodynamics, sediment transport, and vegetation dy-  
19 namics. Tidal channels affect and, at the same time, are affected by the growth of salt  
20 marshes fringing them. The coupled evolution of these morphological units is thus a key  
21 ingredient for simulating the typical behaviour of tidal environments. We developed a  
22 mathematical model accounting for vegetation-induced flow resistance and wetting-drying  
23 processes typical of tidal environments, to investigate the eco-morphodynamic evolution  
24 of intertidal areas fringing a main channel and of the tidal creeks cutting through them.  
25 Model results indicate that vegetation promotes the development of channel networks,  
26 leading to more complex channel structures and higher drainage efficiency. Vegetation  
27 encroachment influences sediment deposition patterns by trapping sediment in the sea-  
28 ward and middle intertidal areas, while reducing the amount of sediment delivered to  
29 landward areas. In the presence of sea level rise, this deficit of sediment enhances the  
30 landward-decreasing trend of the intertidal platform and leads to more isolated vegeta-  
31 tion patches. Overall, sea level rise restricts the extension of salt marshes and consequently  
32 reduces the effect of vegetation on channel development.

## 33 Plain Language Summary

34 Tidal channels in coastal landscapes connect the sea and the landward salt marshes,  
35 acting as essential drainage pathways for exchanging water, sediments, and nutrients.  
36 The effect of vegetation on channel morphology strongly influence the morphodynamic  
37 evolution of the intertidal zone. In this study, a tide-dominated intertidal basin is sim-  
38 ulated through a numerical model to analyze the mutual relations between vegetation  
39 growth and channel development. Vegetation better suited to live at lower elevations strongly  
40 promotes channel development, creating a more efficient drainage system. As the sea-  
41 ward vegetation patches trap the sediment coming from the sea, less sediment is trans-  
42 ported to the landward areas, leading to a lower landward deposition rate. Furthermore,  
43 sea-level rise restricts vegetation growth and thus reduces the effects of vegetation on  
44 tidal channel development.

## 45 1 Introduction

46 Tidal flats and salt marshes connect the land and the ocean by mediating the ex-  
47 change of water, sediments and nutrients within coastal landscapes (Mitsch & Gosselink,  
48 2000; Zedler & Kercher, 2005; FitzGerald & Hughes, 2019). Salt marshes are typically  
49 covered by halophytic vegetation. They occupy elevations higher than mean sea level (MSL)  
50 and are periodically inundated by the tide (Allen, 2000; Friedrichs & Perry, 2001). Con-  
51 versely, tidal flats lie below mean sea level and, hence, are intermittently exposed dur-  
52 ing low tides (Zhou et al., 2016). They do not host halophytic vegetation, but can be  
53 covered by microbial biofilms or colonized by sea grasses which contribute to stabilize  
54 the sediment bed (Yallop et al., 1994; Chen et al., 2017).

55 Depending on the rate of relative sea level rise (RSLR) and sediment availability,  
56 tidal flats can evolve into salt marshes and vice versa (Fagherazzi et al., 2006; Marani  
57 et al., 2007; Zhou et al., 2016). As the elevation of the intertidal platform increases within  
58 the tidal frame, flow conditions become suitable for the settlement of vegetation seeds.  
59 The bare surface of tidal flats is thus progressively encroached by vegetation patches, and  
60 eventually a salt marsh forms as a result of the interaction of physical and biological pro-  
61 cesses (Bouma et al., 2014; Hu et al., 2015). On the contrary, a salt marsh can experi-  
62 ence a transition into a tidal flat when marsh accretion rate is lower than the rate of RSLR,  
63 and the marsh platform progressively drowns (Kirwan et al., 2010; D’Alpaos et al., 2011).  
64 The window of opportunity (Balke et al., 2011, 2014; Hu et al., 2015) for vegetation growth

65 is reduced and vegetation progressively disappears (Morris et al., 2002; Kirwan & Megonigal, 2013). Salt marshes can also undergo a transition into tidal flats through lateral  
66 retreat of marsh edges. These edges are characterized by scarps between the vegetated  
67 marsh surface and the bare tidal flat bottom facing the marsh. Wind waves impinge against  
68 salt marsh edges, leading to marsh lateral retreat, and erode sediments from the tidal  
69 flats, promoting their deepening (e.g. Marani et al., 2011; Mariotti & Fagherazzi, 2013;  
70 Leonardi & Fagherazzi, 2014; Leonardi et al., 2016). Deeper and wider tidal flats favor  
71 the development of stronger wind waves (Mariotti & Fagherazzi, 2013; Tommasini et al.,  
72 2019) and, consequently, enhance wave-induced erosion of the salt marsh border (Bendoni  
73 et al., 2016).  
74

75 The evolution of tidal flats and salt marshes is strongly related to tidal channel dy-  
76 namics. Both tidal channel and intertidal platform evolution are governed by the inter-  
77 actions between hydrodynamics, sediment transport, morphological changes, and bio-  
78 logical effects (D’Alpaos et al., 2007; Temmerman et al., 2007; De Swart & Zimmerman,  
79 2009; Vandenbruwaene et al., 2011; Gong et al., 2018; Zhao et al., 2019; Li et al., 2019).  
80 The mutual feedbacks (either positive or negative), which characterize these interactions,  
81 control the so-called *Morphodynamic Loop* (Wright & Thom, 1977; Cowell & Thom, 1994;  
82 Coco et al., 2013). Given proper initial and boundary conditions, the overall evolution  
83 of tidal systems is controlled by the interplay between the various morphological units  
84 (tidal channels, tidal flats and salt marshes). Tidal channels act as preferential drainage  
85 pathways (D’Alpaos et al., 2005; Hughes, 2012; Coco et al., 2013; Zhou et al., 2014) and,  
86 hence, regulate sediment distribution within the tidal system. In addition, sediment avail-  
87 ability determines the fate of tidal flats and salt marshes in response to increasing sea  
88 levels and wave-induced lateral erosion (Mariotti & Fagherazzi, 2013). In turn, intertidal  
89 platform elevation within the tidal frame controls the tidal prism, ultimately determin-  
90 ing the size and extent of tidal channel networks (e.g. D’Alpaos et al., 2006; van der We-  
91 gen et al., 2010; Stefanon et al., 2012; Kleinhans et al., 2015).

92 Vegetation dampens tidal flow energy and strengthens the soil through the roots.  
93 Vegetation thus reduces erosional processes and enhances sediment deposition through  
94 trapping and organic soil production (Toy et al., 2002; Temmerman et al., 2005; Mudd  
95 et al., 2010; D’Alpaos & Marani, 2016). In the early stages of salt marsh formation, the  
96 flow concentration favored by pioneering vegetation patches causes erosion and channel  
97 initiation (Temmerman et al., 2007; Vandenbruwaene et al., 2011; Temmerman et al.,  
98 2012; Van Oyen et al., 2014). On the surface of fully-colonized salt marshes, the increased  
99 flow resistance leads to flux concentration within channels, enhancing their initiation and  
100 further incision (Temmerman et al., 2007). However, the reduction experienced by the  
101 tidal prism as marsh elevation increases leads to weaker in-channel currents and coun-  
102 teracts channel scouring (D’Alpaos et al., 2006). The elevation of the intertidal platform  
103 in the tidal frame, in turn, dictated by sediment availability and the rate of RSLR, con-  
104 trols which effect prevails over the other (Sgarabotto et al., 2021). In general, the width-  
105 to-depth ratio of salt marsh channels is smaller than that of channels cutting through  
106 tidal flats (Marani et al., 2002; Fagherazzi et al., 2004; Lawrence et al., 2004; D’Alpaos  
107 et al., 2005; Vandenbruwaene et al., 2012; Sgarabotto et al., 2021).

108 RSLR adds a further degree of complexity. The growth of halophytic vegetation  
109 depends on bed elevation within the tidal frame (Morris et al., 2002; Mudd et al., 2004).  
110 Long periods of submergence are unsuitable for the survival of halophytic plants because  
111 of the poor soil aeration. Therefore, high rates of RSLR threaten the survival of salt marshes  
112 (Marani et al., 2007; Kirwan & Temmerman, 2009; Coco et al., 2013) and can prevent  
113 their development. These morphological units can thus keep pace with the increasing  
114 sea levels only if sediment supply and organic soil production by vegetation are high enough  
115 to counterbalance the effects of RSLR (Pilkey & Cooper, 2004; Kirwan et al., 2010; D’Alpaos  
116 et al., 2011; Lovelock et al., 2011).



**Figure 1.** Typical examples of intertidal areas flanking a main tidal channel/river: a) Bare tidal flats on Warbah Island, N29°57'20"-E48°02'05" (Kuwait); b) Salt marsh along the Dell'Ancora Channel, N45°31'06"-E12°28'52" (Venice Lagoon, Italy); c) Salt marsh at the mouth of River Great Ouse, N52°48'04"-E00°21'23" (United Kingdom); d) Salt marsh along the Petaluma River, N38°07'39"-W122°30'42" (California, USA). Source: Google Earth.

117 Only a few studies simulate the intertwined eco-morphodynamic evolution of salt  
 118 marshes and tidal channels cutting through them (D'Alpaos et al., 2007; Temmerman  
 119 et al., 2007; Belliard et al., 2015; Mariotti, 2018; Sgarabotto et al., 2021), accounting for  
 120 the mutual interactions among these morphological units. In this contribution, we un-  
 121 ravel the relative importance of biogeomorphic feedbacks through the analysis of the evo-  
 122 lution of a tidal environment composed by narrow intertidal areas flanking large tidal  
 123 channels or tidal rivers. Some examples of this type of tidal environments are shown in  
 124 Figure 1. Typically, a series of almost evenly spaced channels, directed perpendicularly  
 125 to the main channel, feed and drain the considered intertidal area, consisting either of  
 126 bare tidal flats (Figure 1a) or salt marshes (Figures 1b-d).

127 Starting from an initially flat intertidal platform, we simulate the evolution of the  
 128 system under the action of prescribed tidal forcing, sediment input and sea level rise. Veg-  
 129 etation is assumed to encroach the platform as a reference threshold elevation is exceeded.  
 130 Vegetation patches then develop in a dynamic bed topography characterized by extend-  
 131 ing tidal channels. Vegetation feedbacks on tidal channel structure are elucidated by com-  
 132 paring the morphologies computed in the presence of vegetation with those obtained con-  
 133 sidering the evolution of bare tidal flats subjected to the same forcings.

134 The rest of the paper is structured as follows. Section 2 describes the model de-  
 135 veloped for the analysis of the eco-morphodynamic evolution of the considered systems  
 136 and the design of the numerical simulations. Section 3 reports the numerical results in  
 137 terms of bed topographies, spatial distributions of vegetation biomass, mean erosion/deposition  
 138 rates, and tidal channel features. These results are discussed in Section 4 with specific

139 attention to the effects of RSLR, the comparison with field data, and the limitations in-  
 140 trinsic to the modeling approach. Finally, Section 5 is devoted to the conclusions.

## 141 2 Material and Methods

### 142 2.1 Model Setup

143 The proposed eco-geomorphic model includes four modules to simulate the inter-  
 144 actions among the three main morphological units (tidal channels, tidal flats, and salt  
 145 marshes) which generally compose a tidal basin. The different modules deal with tidal  
 146 currents, sediment transport, bed evolution, and vegetation growth. Before describing  
 147 in detail these modules, it is worth briefly describing how the modules are related to each  
 148 other.

149 Essentially, we assume that hydrodynamics and bed evolution are characterized by  
 150 different temporal scales. In other words, the flow field is taken to adapt almost instan-  
 151 taneously to changes in bed elevation. These latter changes, in fact, are supposed to be  
 152 relatively smooth in space and to need several tidal cycles for exerting their feedback on  
 153 the flow field. At each time step of a characteristic tidal cycle, stemming from the pre-  
 154 scribed tidal forcing, the spatial distribution of flow velocity is used to solve the advection-  
 155 dispersion equation for the suspended sediment concentration. At the same time, cumu-  
 156 lative erosion/deposition rates are computed at each bed location based on the spatial  
 157 distribution of bed shear stresses exerted by the flow. In the presence of vegetation, trap-  
 158 ping of sediment and organic soil production are accounted for in the computation of de-  
 159 position, while erosion is taken to be negligible. Vegetation biomass, which is computed  
 160 as a function of bed elevation, modifies the friction term in the hydraulic module. At the  
 161 end of any characteristic tidal cycle, the bed elevation is updated by employing the tidally  
 162 averaged erosion/deposition rates multiplied by a morphological factor. The character-  
 163 istic tidal cycle is then repeated.

#### 164 2.1.1 Hydraulic module

We consider an intertidal basin dominated by tidal forcing. As a first approxima-  
 tion, wind action and possible river inflows are not considered. The flow field is described  
 through a suitably simplified version of the two-dimensional (2D) depth-averaged mo-  
 mentum and mass conservation equations developed by Defina (2000) to account for wet-  
 ting and drying processes. At each instant  $t$  of the tidal cycle, the free surface elevation  
 $h$  is assumed to be given by the sum of a constant contribution  $\xi$ , coinciding with the  
 water elevation prescribed at the seaward boundary, and a variable contribution,  $\zeta$ , which  
 expresses the local variation of the free surface with respect to the average water level  
 (Figure 2), namely:

$$h(x, y, t) = \xi(t) + \zeta(x, y, t), \quad (1)$$

165 where  $x$  is the landward directed cartesian coordinate, with origin at the seaward bound-  
 166 ary and  $y$  is the transverse cartesian coordinate. Both the quantities  $h$  and  $\zeta$  are referred  
 167 to MSL.

Owing to the relatively small flow depths typical of the investigated flows, friction  
 is assumed to prevail over inertia and, consequently, to balance the free surface slope in  
 the momentum equations (Rinaldo et al., 1999; D'Alpaos et al., 2007). By evaluating  
 the bed shear stress through the Gauckler-Strickler resistance law, it is easily demon-  
 strated that the mass and momentum conservation equations take the form

$$\psi \frac{\partial h}{\partial t} + \frac{\partial (D U_x)}{\partial x} + \frac{\partial (D U_y)}{\partial y} = 0, \quad (2)$$

$$\frac{\partial h}{\partial x} = - \frac{U_x \sqrt{U_x^2 + U_y^2}}{K_s^2} \left( \frac{D}{\phi} \right)^2, \quad (3)$$

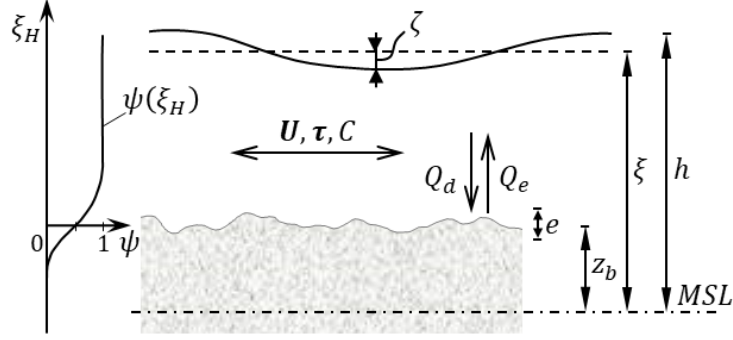


**Figure 2.** Sketch of the flow field and relevant notations.

$$\frac{\partial h}{\partial y} = -\frac{U_y \sqrt{U_x^2 + U_y^2}}{K_s^2} \left(\frac{D}{\phi}\right)^2, \quad (4)$$

168 with

$$D = \frac{e}{4} \left[ \frac{1}{\sqrt{\pi}} \exp(-\xi_H^2) - \xi_H \operatorname{erfc}(\xi_H) \right], \quad (5)$$

$$\psi = \frac{1}{2} \operatorname{erfc}(\xi_H), \quad (6)$$

$$\phi = \left[ D + 0.27 \sqrt{e D} \exp(-2 D/e) \right]^{5/3}. \quad (7)$$

Here,  $U_x$  and  $U_y$  are the longitudinal and transverse components of the depth-averaged velocity, respectively;  $D$  is the effective water depth;  $K_s$  is the Gauckler-Strickler resistance coefficient;  $\psi$  and  $\phi$  are two functions (the first dimensionless) arising from the depth-averaging of the relevant equations over a representative elementary area to account for wetting and drying effects (Defina, 2000), and  $\operatorname{erfc}$  is the complementary error function. The quantities  $D$ ,  $\psi$ , and  $\phi$  depend on the dimensionless variable

$$\xi_H = -2 \frac{h - z_b}{e}, \quad (8)$$

169 where  $z_b$  is the bed elevation referred to MSL and  $e$  is a characteristic scale of variations  
 170 of bed elevation over the representative elementary area (i.e. a subgrid averaged rough-  
 171 ness).

172 Note that the method chosen here to deal with wetting/drying processes allows one  
 173 to always solve the same set of equations, without the need of removing/adding elements  
 174 as the domain gets wet/dry. If the water level is much higher than the bed level, the ef-  
 175 fective water depth becomes equal to the local flow depth  $h - z_b$ . Conversely, if  $h - z_b$   
 176 is very small (even negative if the bed gets dry),  $D$  approaches a very small positive value  
 177 that simulates a partially-wet condition.

178 Recalling the definition of the free surface elevation (1), the simplified momentum  
 179 equations (3) and (4) can be rewritten in the form

$$U_x = -\frac{K_s^2}{\sqrt{U_x^2 + U_y^2}} \left(\frac{\phi}{D}\right)^2 \frac{\partial \zeta}{\partial x}, \quad (9)$$

$$U_y = -\frac{K_s^2}{\sqrt{U_x^2 + U_y^2}} \left(\frac{\phi}{D}\right)^2 \frac{\partial \zeta}{\partial y}. \quad (10)$$

Substituting these expressions into (2), and setting  $U = \sqrt{U_x^2 + U_y^2}$ , we obtain the following equation (Van Oyen et al., 2014)

$$\psi \left( \frac{d\xi}{dt} + \frac{\partial \zeta}{\partial t} \right) - \left[ \frac{\partial}{\partial x} \left( \frac{K_s^2 \phi^2}{U D} \frac{\partial \zeta}{\partial x} \right) + \frac{\partial}{\partial y} \left( \frac{K_s^2 \phi^2}{U D} \frac{\partial \zeta}{\partial y} \right) \right] = 0, \quad (11)$$

180 that describes the spatio-temporal variation of the water level  $\zeta(x, y, t)$  given the water  
181 elevation at the seaward boundary  $\xi$ .

182 Equation (11) is solved numerically through finite differences. The spatial deriva-  
183 tives are discretized through central differences, while forward differences are employed  
184 for the temporal derivative  $\partial \zeta / \partial t$ . The resulting system of equations is solved with the  
185 open-source computational package ‘‘Pardiso’’. At each time step, Picard iteration is used  
186 to deal with the nonlinear terms involving  $U$ . At the first iteration,  $U$  is set equal to the  
187 magnitude of the velocity at the previous time step. After solving for  $\zeta$ , at the next it-  
188 eration,  $U$  is updated based on the values of  $U_x$  and  $U_y$  given by equations (9) and (10),  
189 respectively. The iteration stops when the percentage difference between the values of  
190  $\zeta$  computed at previous and current iterations is less than a prescribed small value (5  
191 %).

192 The boundary conditions associated with the system of partial differential equa-  
193 tions (9), (10), and (11) consist of the water level at the sea boundary, where  $\xi$  is taken  
194 equal to a cosine tidal wave with amplitude  $a_0$ , while no-flux conditions are imposed at  
195 the other boundaries of the simulated tidal basin. The geometry of this domain is de-  
196 scribed below, in the paragraph concerning the design of numerical experiments.

197 At the initial instant of any simulation, a constant water level is prescribed through-  
198 out the basin at high water slack, equal to the high tide level, while the flow velocity is  
199 set everywhere to zero. The simulation thus starts with the ebb phase.

### 200 **2.1.2 Sediment transport**

Sediments are assumed to be transported mainly as suspended load, owing to their fine size. Their dynamics is described by the two-dimensional advection-dispersion equation (e.g. D’Alpaos et al., 2007)

$$\frac{\partial(CD)}{\partial t} + \nabla(CD\mathbf{U} - k_m D \nabla C) = Q_e - Q_d, \quad (12)$$

201 where  $C$  is the depth-averaged suspended sediment concentration,  $\mathbf{U}$  is the depth-averaged  
202 velocity vector,  $k_m$  is the horizontal mixing coefficient, and  $Q_e$  and  $Q_d$  are the rate of  
203 erosion and deposition, respectively. Equation (12) is solved numerically by an explicit  
204 central difference method.

205 During the flood phase, a given external suspended sediment concentration  $C_{sea}$   
206 is imposed at the seaward boundary of the tidal basin. Conversely, during the ebb phase  
207 sediments are transported out of the tidal basin. The suspended sediment concentration  
208 at the seaside boundary is thus determined by the sediment concentration coming from  
209 upstream. According to these boundary conditions, the suspended sediment is conveyed  
210 into the tidal basin and redistributed therein by the flood currents. Conversely, ebb cur-  
211 rents usually tend to flush out the sediment. Finally, at the beginning of the simulation,  
212 the suspended sediment concentration within the basin is taken to linearly decrease from  
213  $C_{sea}$  at the seaward boundary to  $0 \text{ g/m}^3$  at the landward boundary.

### 214 **2.1.3 Bed evolution**

Local erosion and deposition drive bed evolution of the channeled and unchanneled portions of the basin. The contribution of bedload to bed evolution is assumed to be much



smaller than the contribution of suspended load. Bed-elevation changes are described through the sediment balance equation (e.g., Marani et al., 2007; Toffolon & Lanzoni, 2010)

$$\frac{\partial z_b}{\partial t} = Q_e - Q_d - R. \quad (13)$$

215 where  $Q_e$  and  $Q_d$  are the erosion and deposition rates, respectively and  $R$  is the  
216 rate of RSLR.

217 The erosion flux  $Q_e$  is determined on the basis of the excess of the shear stress mod-  
218 ulus  $\tau$  with respect to the critical stress  $\tau_{ce}$ . Conversely, the deposition flux in general  
219 depends on the settling velocity and on the magnitude of suspended sediment as clar-  
220 ified in the following.

At each location of the tidal basin the modulus of  $\tau$  is computed as  $\sqrt{\tau_x^2 + \tau_y^2}$ , where the components  $\tau_x$  and  $\tau_y$  of the bed shear stress vector are determined by considering the local flow depth and the local free surface slope, namely

$$\tau_x = -\rho g D \frac{\partial \zeta}{\partial x}, \quad \tau_y = -\rho g D \frac{\partial \zeta}{\partial y}. \quad (14)$$

The erosion rate is eventually computed as

$$Q_e = Q_{e0} \left\{ -1 + \left[ 1 + \left( \frac{\tau}{\tau_{ce}} \right)^4 \right]^{1/4} \right\} \quad (15)$$

221 where  $Q_{e0}$  is a typical intensity of erosion flux, depending on the type of sediment com-  
222 posing the bed. Note that equation (15) ensures a smooth transition from no-erosion to  
223 erosion conditions. This formulation, introduced by Carniello et al. (2012), prevents strong  
224 gradients of the erosion rate in a neighbourhood of the critical threshold  $\tau_{ce}$ , thus en-  
225 suring a more gradual reproduction of scour processes.

The deposition rate is expressed as (D'Alpaos et al., 2007)

$$Q_d = Q_{ds} + Q_{dt} + Q_{do} \quad (16)$$

226 where  $Q_{ds}$ ,  $Q_{dt}$  and  $Q_{do}$  are the rates of deposition due to settling, vegetation trapping,  
227 and organic soil production, respectively. Settling deposition at any shear stress value  
228 is computed as

$$Q_{ds} = C w_s \quad (17)$$

229 where  $w_s$  is the settling velocity of sediment particles.

230 On the other hand, trapping deposition and organic deposition are related to veg-  
231 etation biomass, as described below.

#### 2.1.4 *Vegetation growth*

The local annually-averaged biomass production is expressed through a fitness function (Marani et al., 2013), which describes the relationship between the local bed elevation  $z_b$  and the biomass density  $\mathcal{B}$ ,

$$\frac{\mathcal{B}(z_b)}{\mathcal{B}_{max}} = b(z_b) = \frac{f(z_b)}{f_{max}}, \quad (18)$$

where  $\mathcal{B}_{max}$  is the maximum biomass density,  $b(z_b)$  is the dimensionless biomass density,  $f(z_b)$  is a fitness function and  $f_{max}$  is its maximum value. The fitness function is

species specific. Here, following Marani et al. (2013), the fitness function is described through the relation,

$$f(z_b) = \frac{2}{e^{[\lambda_1(z_b - z_{0v})]} + e^{[-\lambda_2(z_b - z_{0v})]}}, \quad (19)$$

233 where the elevation parameter  $z_{0v}$  corresponds to the optimal elevation for vegetation  
 234 growth (i.e. at which the maximum biomass is attained), and the dimensional param-  
 235 eters,  $\lambda_1$  [ $\text{m}^{-1}$ ] and  $\lambda_2$  [ $\text{m}^{-1}$ ], control the range of bed elevations to which vegetation is  
 236 adapted. Large values of  $\lambda$  are typical of specialized vegetation species, that fit within  
 237 a narrow range of elevations. Conversely, small values of  $\lambda$  characterize species which  
 238 are relatively well adapted to a broader range of marsh elevations within the tidal frame.

Vegetation patches influence the flow field by modifying the resistance to the flow. A higher biomass density leads to higher friction and, hence, a lower resistance coefficient. The overall bed friction is then assumed to be given by the sum of the local bed friction and the friction induced by the vegetation. This overall bed friction is inversely proportional to the square of a total Gauckler-Strickler resistance coefficient and is expressed as

$$K_s^{-2} = K_{sb}^{-2} + b K_{sv}^{-2}, \quad (20)$$

239 where  $K_{sb}$  and  $K_{sv}$  are the Gauckler-Strickler coefficients related to bed friction and veg-  
 240 etation, respectively.

241 Vegetation patches also influence bed evolution by trapping suspended sediment,  
 242 through stems and leaves, and producing organic soil (the last two terms in equation (16)).  
 243 Based on the approach of Mudd et al. (2004), Palmer et al. (2004), and D'Alpaos et al.  
 244 (2006), these contributions to the rate of variation of bed elevation can be expressed as

$$Q_{do} = Q_{do0} b(z_b), \quad (21)$$

$$Q_{dt} = C U \epsilon_v d_v n_v \min[h_v; D], \quad (22)$$

where  $Q_{do0}$  is a typical deposition rate specified empirically and  $\epsilon_v$  is a capture efficiency coefficient (Palmer et al., 2004). This latter coefficient can in general be related to the diameter  $d_v$ , the density  $n_v$  and the average height  $h_v$  of vegetation stems, as well as to the median suspended sediment size  $d_{50}$  through the relation (D'Alpaos et al., 2006)

$$\epsilon = \alpha_\epsilon \left( \frac{U d_v}{\nu} \right)^{\beta_\epsilon} \left( \frac{d_{50}}{d_v} \right)^{\gamma_\epsilon} \quad (23)$$

245 with  $\alpha_\epsilon$ ,  $\beta_\epsilon$  and  $\gamma_\epsilon$  empirical coefficients.

Finally, the values of the diameter, the density and the average height of vegetation stems can be estimated on the basis of local vegetation biomass through the empirical relations (Mudd et al., 2004, 2010)

$$n_v = \alpha_n \mathcal{B}^{\beta_n}, \quad h_v = \alpha_h \mathcal{B}^{\beta_h}, \quad d_v = \alpha_d \mathcal{B}^{\beta_d}. \quad (24)$$

246 where  $\alpha_n$ ,  $\beta_n$ ,  $\alpha_h$ ,  $\beta_h$ ,  $\alpha_d$  and  $\beta_d$ , are empirical coefficients.

## 2.2 Design of numerical experiments

247  
 248 In this research, we focus on the interactions between tidal channels and vegeta-  
 249 tion patches that form on a tide-dominated tidal flat of relatively small dimensions, i.e.  
 250 400 m wide and 500 m long. Figures 3a-c show the initial bed topography, assumed to  
 251 be horizontal with small perturbation patches and with a base elevation of 0 m above  
 252 MSL. The basin is connected with a deep and large tidal channel at the seaward bound-  
 253 ary. A square computational grid of size 2 m is used to discretize the relevant equations.

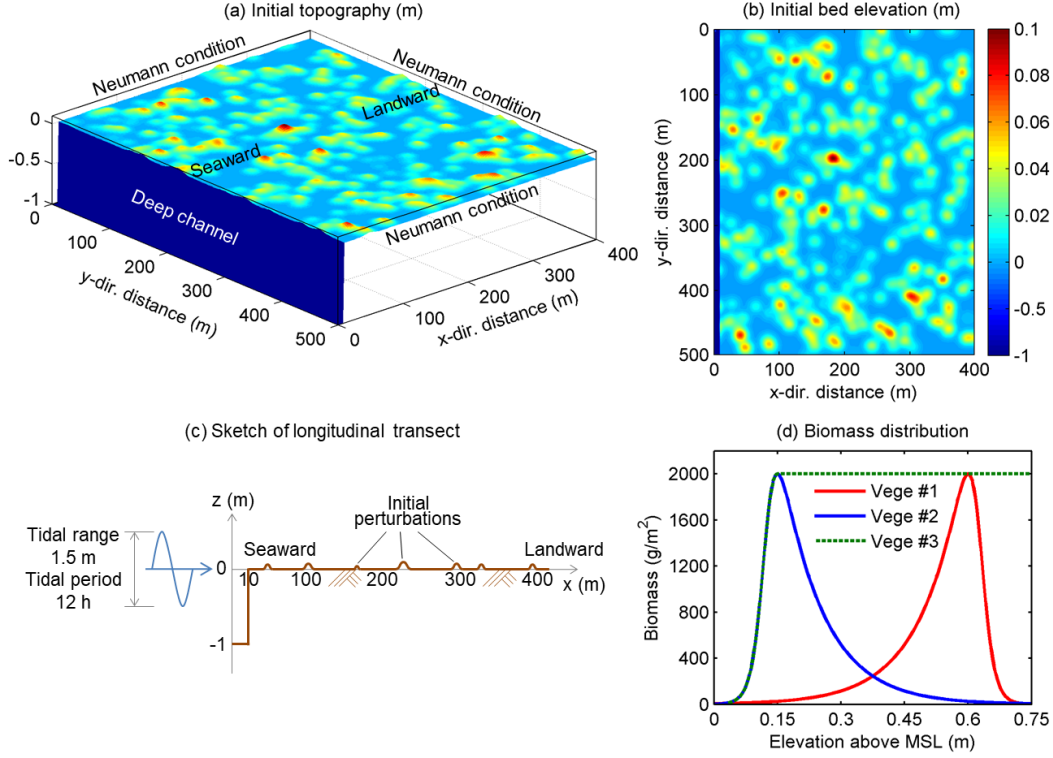


**Figure 3.** a) Three-dimensional view, b) planform view and c) longitudinal transect of the initial bed topography employed in the present simulations. d) Biomass distribution mimicking three different types of salt-marsh vegetation species.

254 The initial perturbation patches (in total 450) are generated on a horizontal bed  
 255 and are meant to mimic the initial settlement of vegetation patches (Figures 3a,b). The  
 256 location and magnitude of these perturbations are determined by a stochastic procedure.  
 257 Firstly, the location ( $x, y$ ) of each perturbation is selected randomly. Secondly, a ran-  
 258 dom height is imposed at each perturbation location. Then, the elevation around the se-  
 259 lected point is averaged iteratively to generate a perturbation patch with a smoothly vary-  
 260 ing surface. This procedure is repeated a certain number of times (15 in the considered  
 261 case) to expand the patch extension while reducing the patch height, eventually produc-  
 262 ing relatively isolated perturbation patches. Finally, the maximum elevation of the re-  
 263 sulting bed topography is set equal to 0.1 m, and the height of other points is adjusted  
 264 proportionally. Note that this stochastic procedure leads also to the formation of clus-  
 265 tered patches (Figure 3b).

266 The water level imposed at the seaward boundary reproduces a semi-diurnal tidal  
 267 cycle of period 12 h and amplitude 0.75 m with respect to MSL (set at 0 m). A no-flux  
 268 condition is instead prescribed on the other three boundaries of the basin. A sediment  
 269 concentration  $C_{sea}$  of  $10 \text{ g/m}^3$  is imposed at seaward boundary during the flood phase  
 270 of the tide, to mimic an external input of sediment. This input is in general associated  
 271 with isolated recurrent events (e.g. wind resuspension, spring tides, floods in river nour-  
 272 ished environments) but, in the long term, can be modeled imposing a constant (aver-  
 273 age)  $C_{sea}$  as done here.

274 Because of the significant elevation drop that, during the ebb phase, establishes be-  
 275 tween the tidal flat and the seaward tidal channel feeding the system (see e.g. Figure 2),  
 276 extensive erosion spots may take place at the beginning of the morphodynamic evolu-

277 tion. In order to mitigate these localized phenomena, which may lead to numerical in-  
 278 stabilities, the amplitude of the forcing tide is gradually increased from 0 m to 0.75 m  
 279 within the first 800 tidal cycles.

Typically, a control section forms nearby the seaward border of the tidal basin as the ebb level of the forcing tide becomes smaller than bed elevation (Figure 3c). This section is characterised by a Froude number  $F_r$  equal to 1 and disconnects the tidal basin from the seaward channel feeding it. Given this control section, upstream (i.e. landwards) the flow is subcritical ( $F_r < 1$ ), while downstream (i.e. seawards) it is supercritical ( $F_r > 1$ ). The tide level at the seaward boundary thus no longer influences the ebb current still flowing within the tidal basin. The ebb flow is instead controlled by the condition  $F_r = 1$  that establishes in the control section. It is thus necessary to modify the seaward boundary condition, by limiting to 1 the corresponding Froude number. During the ebb phase, the effective water depth at the seaward boundary  $D_{sea}$  is then prescribed as

$$D_{sea}^{i+1} = \frac{|U_{sea}^i|^2}{0.9g}, \quad \text{If} \quad F_{r\,sea}^i = \frac{|U_{sea}^i|}{\sqrt{gD_{sea}^i}} > 0.9, \quad (25)$$

280 where the superscript  $i$  indicates the  $i$ -th time step and it has been assumed, for com-  
 281 putational convenience, that the Froude number at the boundary can be at maximum  
 282 equal to 0.9. The condition (25) is retained also during the flood phase until the level  
 283 of the imposed tide exceeds that of the seaward basin border. Henceforth, the flow be-  
 284 comes subcritical everywhere and, hence, is completely controlled by the imposed tidal  
 285 wave level.

286 As widely adopted in long-term simulations (Roelvink, 2006; Coco et al., 2013),  
 287 a morphological factor is used to speed up morphodynamic evolution. After each sim-  
 288 ulated tidal cycle, the elevation of each computational grid point is first updated through  
 289 equation (13) and then multiplied by a morphological factor, set equal to 40 after some  
 290 preliminary tests.

291 Three different types of vegetation have been considered in the simulations (Fig-  
 292 ure 3d). All vegetation types start to grow as bed elevation exceeds MSL and survive  
 293 up to mean high water level (MHWL). The first vegetation type (Vege #1) is better adapted  
 294 to grow at high elevations. Its biomass increases relatively slowly and reaches a maxi-  
 295 mum at 0.60 m above MSL. Then biomass decreases rapidly as bed elevation increases,  
 296 eventually vanishing as MHWL is approached. The second vegetation type (Vege #2)  
 297 is better adapted to grow at low elevations. Its biomass production peaks at 0.15 m above  
 298 MSL, i.e. close to MSL, and gradually vanishes towards MHWL. Finally, the third veg-  
 299 etation type (Vege #3) is taken to reproduce biomass distribution in the presence of co-  
 300 existing vegetation species with optimal biomass production occurring at progressively  
 301 higher bed elevations (D’Alpaos et al., 2007; Marani et al., 2007). Just above MSL, the  
 302 biomass function is similar to that of Vege #2. However, after the maximum biomass  
 303 production is attained (at 0.15 m above MSL), biomass keeps constant.

304 It is important to note that vegetation seeds cannot settle in areas undergoing in-  
 305 tense erosion and, hence, halophytic vegetation is significantly endangered in these ar-  
 306 eas. Therefore, in present simulations, the local biomass is set to 0 where erosion is stronger  
 307 than deposition. The values of the physical and empirical parameters adopted in the var-  
 308 ious simulations are listed in Table 1. Finally, although the parameters for Vege #3 are  
 309 the same as Vege #2, in the case of Vege #3, the dimensionless biomass density is kept  
 310 fixed and equal to 1 (green dashed line in Figure 3d) for bed elevations higher than the  
 311 optimal one (0.15 m).

312 During the morphodynamic evolution of the basin, tidal channels cut through both  
 313 tidal flats and salt marshes. The corresponding channelized areas are computed using  
 314 the channel detection method proposed by Geng et al. (2018).

**Table 1.** Values of parameters adopted throughout the simulations

Parameter	Value	Parameter	Value
$\tau_{ce}$	0.4 Pa	$g$	9.81 m/s <sup>2</sup>
$k_m$	0.3 m <sup>2</sup> /s	$w_s$	0.0002 m/s
$Q_{e0}$	0.0002 m/s	$Q_{d00}$	0.003 m/yr
$e$	0.3 m	$d_{50}$	50 $\mu$ m
$K_{sb}$	25 m <sup>1/3</sup> /s	$K_{sv}$	10 m <sup>1/3</sup> /s
$\nu$	0.000001 m <sup>2</sup> /s	$\alpha_\epsilon$	0.224
$\beta_\epsilon$	0.718	$\gamma_\epsilon$	2.08
$\alpha_n$	250 g <sup>-1</sup>	$\beta_n$	0.3032
$\alpha_h$	0.0609 m <sup>3</sup> /g	$\beta_h$	0.1876
$\alpha_d$	0.0006 m <sup>3</sup> /g	$\beta_d$	0.3
$z_{0v}$ , Vege #1	0.6256	$z_{0v}$ , Vege #2, #3	0.1244
$\lambda_1$ , Vege #1	60 m <sup>-1</sup>	$\lambda_1$ , Vege #2, #3	10 m <sup>-1</sup>
$\lambda_2$ , Vege #1	10 m <sup>-1</sup>	$\lambda_2$ , Vege #2, #3	60 m <sup>-1</sup>

### 3 Results

The initiation and development of tidal channels and the accretion of the intertidal platform are simulated for bare soil conditions and for each of the three vegetation types previously introduced. In the following, we summarize the various morphodynamic processes emerging from the simulations.

#### 3.1 Coupled evolution of salt marshes and tidal channels

At the beginning of each simulation, the tidal amplitude is gradually increasing and has not yet reached its final value. The resulting flow field is relatively weak and hence deposition and erosion rates are quite small. As the tidal amplitude approaches its final value (after 800 tidal cycles, i.e. about 1.1 yr), erosional processes amongst bed perturbation patches gradually increase. Tidal channels start to grow from the seaward boundary through headward erosion after about 2.5 yr and a still immature channel network is visible after about 4 yr (Figures 4a,e,i,m). The structure of this incipient network consists of three main channels with similar spacing and, hence, similar drainage areas. This structure is quite similar for all the simulations, independently of the presence and type of vegetation. Indeed, after 4 yr the elevation of the intertidal platform is still too close to MSL and, when vegetation is considered, the biomass is too small to affect significantly channel morphology.

As the sediment enters the tidal basin through the seaward boundary, the elevation of the intertidal platform progressively increases. The suspended sediment concentration decreases landward, owing to deposition induced by settling and by a progressive decrease of advective transport as prescribed by the advection-diffusion equation (12). The high velocities occurring seaward prompt erosion rates higher than deposition ones. Conversely, proceeding landward, velocities become weaker and hence deposition overcomes erosion.

After their initial growth, channels keep deepening and extending landward, leading to more and more structured channel networks. Perturbation patches prompt channels to curve and to branch diverting or splitting their flows, respectively (Figure 4). This general behaviour is enhanced by vegetation. After 12 yr, channel branching and lengthening occur more frequently in the case of Vege #2 and Vege #3, whose biomass can attain high values also during the early stages of the morphodynamic evolution (Figures

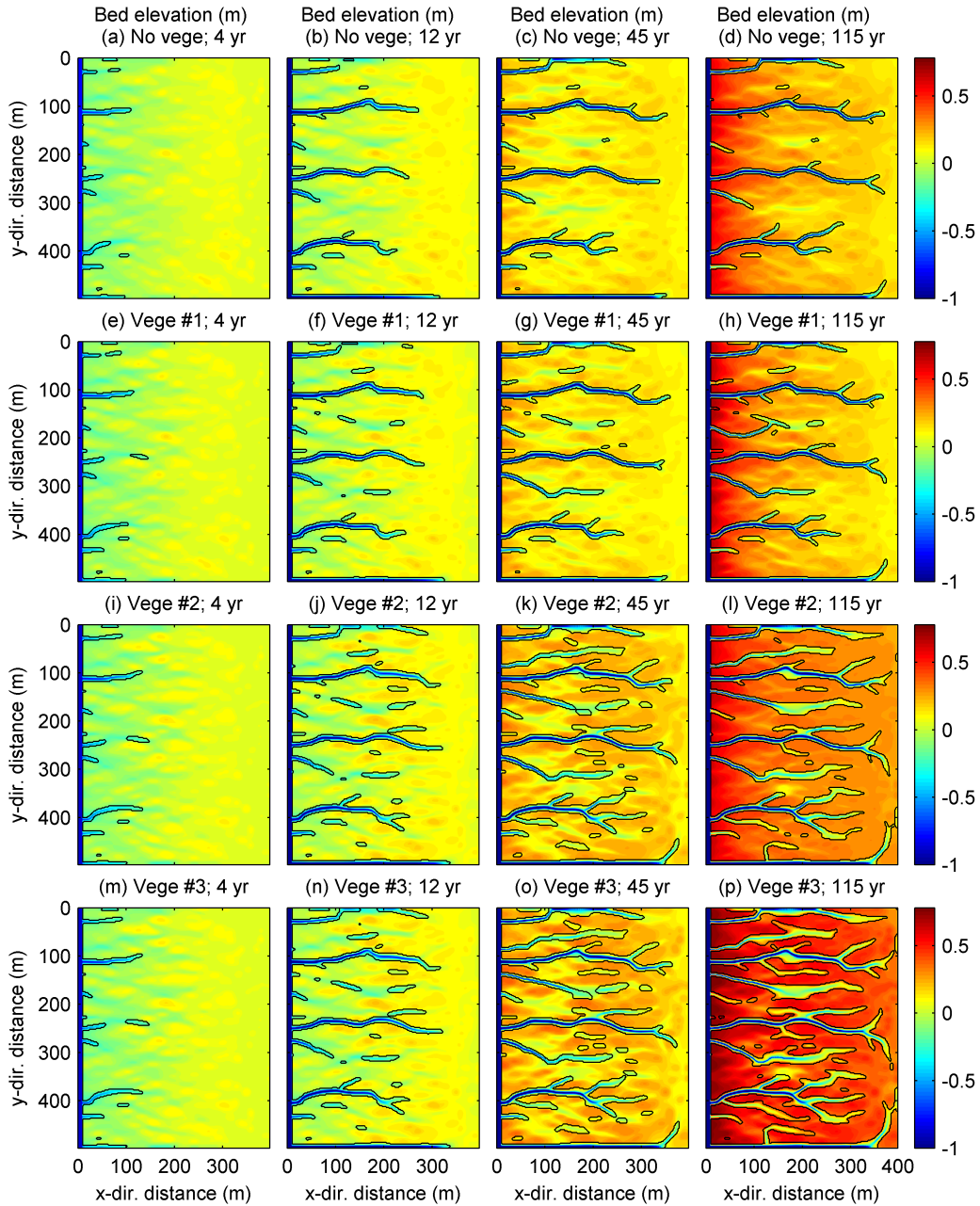


**Figure 4.** The spatial distribution of bed elevations (m), referred to MSL, is plotted at different evolution stages (4, 12, 45, and 115 yr) for the four simulated cases, i.e. in the absence of vegetation (panels a-d) or in the presence of vegetation (Vege #1, panels e-h; Vege #2, panels i-l; Vege #3, panels m-p). Black lines denote the edge of tidal channels.

346 5f-h, and j-l). Conversely, in the case of Vege #1, the optimal bed elevation for biomass  
 347 growth is close to MHWL (Figure 5d) when the channel network has already reached  
 348 a relatively defined configuration. Consequently, the differences with respect to the chan-  
 349 nel network obtained without vegetation are less evident (Figures 4b-d, and f-h).

350 During the bed evolution, platform elevation controls vegetation encroachment and,  
 351 through the adopted biomass parametrization, its effects on morphology. In the case of  
 352 Vege #1, as the mean bed elevation of the tidal basin gradually increases, vegetation first  
 353 starts to encroach seaward areas and then extends landward (Figures 5b-d). This trend  
 354 is qualitatively similar to that observed in Figure 1b. In the cases of Vege #2 and Vege  
 355 #3, biomass production is quite high also during the early stages of evolution, when bed  
 356 elevations are still close to MSL. This allows salt marshes to initially form in the mid-  
 357 dle and landward areas of the tidal basin, where deposition rates exceed erosion rates.  
 358 As the intertidal platform emerges on average and exceeds the optimal elevation for biomass,  
 359 Vege #2, progressively decays (Figures 5f-h). Conversely, Vege #3 gradually spreads through-  
 360 out the tidal basin (Figures 5j-l) enhancing deposition rates. At the end of the evolu-  
 361 tion, the mean elevation of the salt marshes is thus higher as compared to the other cases.

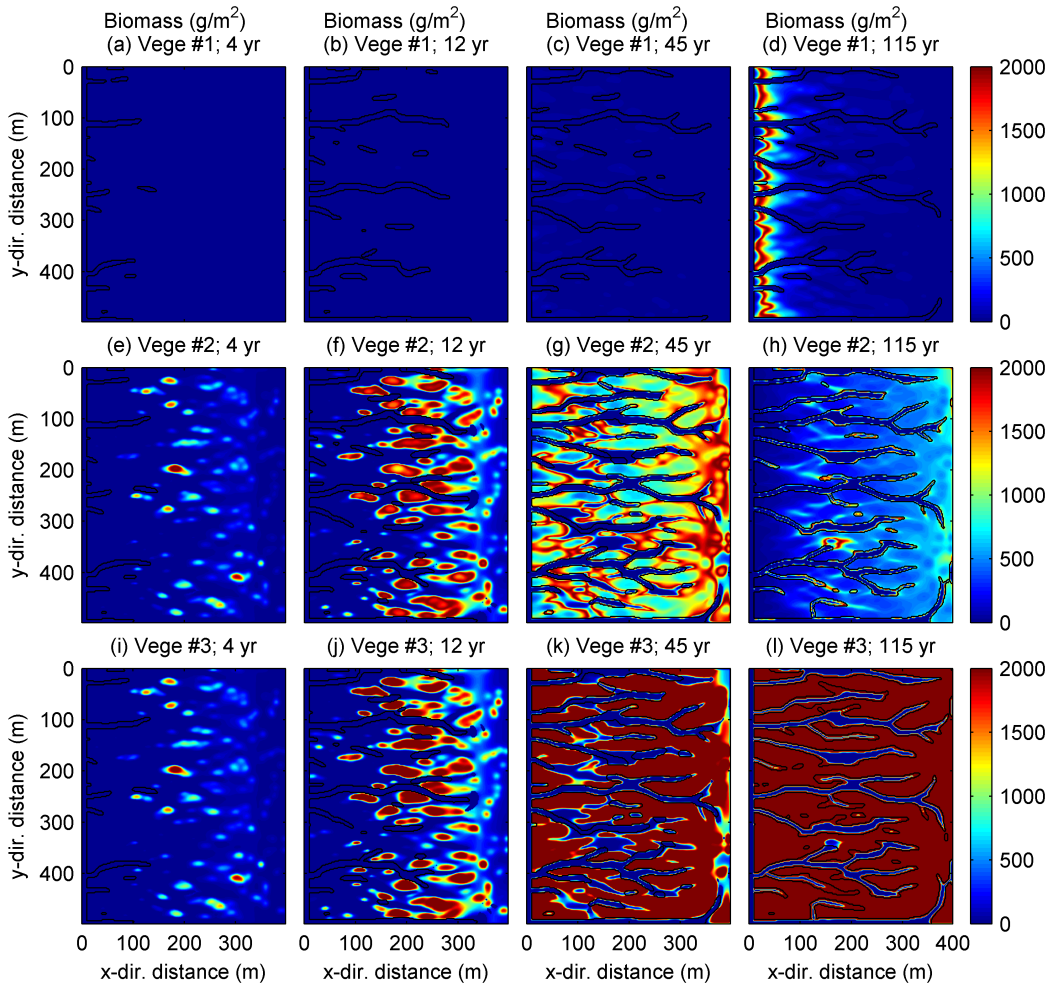


**Figure 5.** The spatial distribution of vegetation biomass ( $\text{g/m}^2$ ) is plotted at different evolution stages (4, 12, 45, and 115 yr) for the three vegetated cases. Vege #1, Panels a-d; Vege #2, panels e-h; Vege #3, panels i-l.

### 3.2 Overall vegetation effects

The overall effects of vegetation on the various morphological units, whether channels, marshes or tidal flats, are here evaluated. To this goal, we tracked the temporal evolution of the total vegetation biomass,  $\mathcal{B}_T$ , the total channel length,  $L_c$ , the volume of the channel network,  $V_c$ , the mean length of unchanneled flow paths,  $\ell$ , the drainage efficiency  $\ell_H/\ell$ , and the cumulative amount of erosion  $\mathcal{E}_r$ .

The total channel length,  $L_c$ , is computed by summing the axis length of all the channels cutting through the tidal basin. The total channel volume is defined as the volume between the channel bed and the elevation of the intertidal platform at the channel borders (Geng et al., 2018). The unchanneled flow path length,  $\ell$ , is computed as the mean distance from a point on the intertidal platform to the nearest channel (Marani et al., 2003). The drainage efficiency is given by the ratio  $\ell_H/\ell$ , with  $\ell_H$  the Hortonian path length given by the ratio of tidal basin area to total channel length (Horton, 1945). For a given Hortonian length,  $\ell_H$ , high values of  $\ell_H/\ell$  correspond to small values of  $\ell$ , indicating that the spatial arrangement of the tidal channels efficiently reduces the mean overmarsh path length (Marani et al., 2003). Finally, the cumulative erosion  $\mathcal{E}_r$  is computed as the total amount of sediment eroded during the evolution.

All the above defined global variables are plotted as a function of time in Figure 6. Both the channel length and the volume of the channel network grow rapidly at the beginning of the evolution (Figures 6a,b). After about 14 yr, as the channels have almost extended throughout the whole tidal basin, the rate of channel lengthening slows down (Figure 6a). As the channels grow landwards, the mean unchanneled length decreases rapidly, eventually tending to a constant value after the total channel length has approached its maximum value (Figure 6c).

The development of vegetation not only promotes channel lengthening (Figure 6a) but also reduces the unchanneled length (Figure 6c). As compared to bare soil conditions, the drainage efficiency of the tidal network increases for vegetation #2 and #3, while it decreases for vegetation #1 (Figure 6d). These findings can be explained by considering the spatial distributions of bed elevation and the channel morphology shown in Figure 4. It emerges that in the case of Vege #1, the final distribution of biomass (Figure 5d) favors the formation of additional channel branches in the seaward and middle portions of the tidal basin (Figure 4h). Conversely, the most landward zones are characterized by a lower degree of channelization, thus leading to a reduction of the overall drainage efficiency of the tidal basin.

In the cases of Vege #2 and Vege #3, the biomass initially reaches quite high values throughout the entire tidal basin (e.g. Figures 5f,j). The tidal channels spread all over the basin and develop many extra branches. Consequently, the drainage efficiency raises (Figure 6d). In particular, the most efficient drainage system is obtained in the case of Vege #3 (Figure 4p) which, at the end of the simulation, exhibits the maximum total biomass as well (Figure 5l). The maximum biomass is approximately four times larger than in the case of Vege #2 (Figure 6d). Indeed, in this latter case, vegetation progressively decays as the bed elevation further accretes after exceeding the optimal level for biomass production. Note that the jumps in drainage efficiency observed for Vege #3 at about 65 yr and 107 yr are associated with the simultaneous headward growth of various channels in the innermost portions of the tidal basin.

It is also worthwhile to note that, during the early stages of evolution (27 yrs), cumulative erosion in the cases of Vege #2 and Vege #3 increases much faster than in the other two cases (Figure 6e). Afterward, differences in cumulative erosion become increasingly smaller and, at the end of the various simulations, tend to vanish. This finding indicates that, even though the final equilibrium configurations of the tidal basin can be



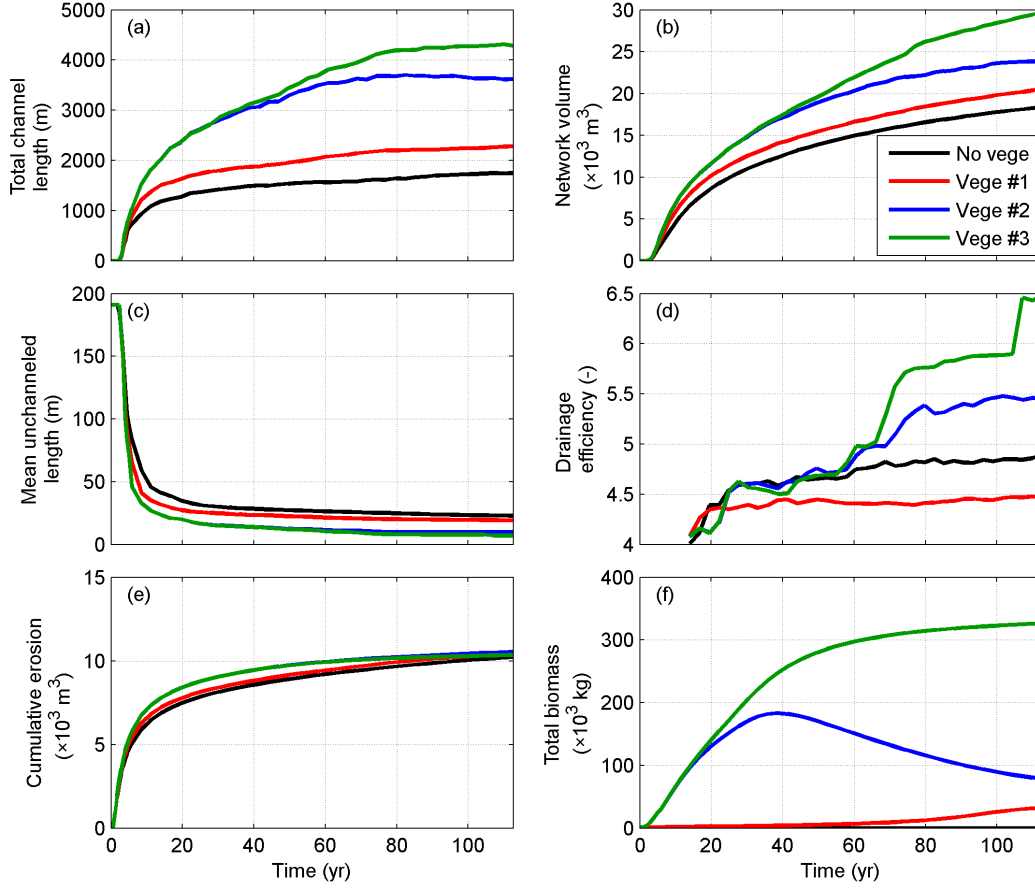


**Figure 6.** a) The total channel length  $L_c$ , b) the total channel volume  $V_c$ , c) the mean unchanneled length  $\ell$ , d) the drainage efficiency  $\ell_H/\ell$ , e) cumulative erosion  $\mathcal{E}_r$  and f) the total biomass  $\mathcal{B}$  are plotted as a function of time for the simulated tidal channel networks. Black lines denote the bare soil case; red, blue, and green lines denote Vege #1, Vege #2, and Vege #3 cases, respectively.

412 characterized by different morphologies (Figure 4), they are obtained with almost the  
 413 same total cumulative erosion.

414 The distribution of vegetation patches influences the evolution and the overall mor-  
 415 phology. The panels in Figures 7a,d,g display the longitudinal variations of mean bed  
 416 elevation in channeled and unchanneled areas. During the early stage of evolution (12 yrs),  
 417 mean unchanneled bed elevations exhibit almost similar trends in all the simulations,  
 418 with an elevation that progressively increases landwards (continuous lines in Figure 7a).  
 419 Later on, the mean elevation of unchanneled areas becomes higher when vegetation patches  
 420 spread throughout the entire basin and the biomass is such to yield a significant produc-  
 421 tion of organic soil (Vege #2 and #3, Figure 7d,g). Conversely, for slowly-growing vege-  
 422 tation patches (Vege #1) the differences with respect to the bare soil case are fairly small.  
 423 Moreover, in the absence of vegetation, the landward portion of the platform is slightly  
 424 higher than in the vegetated cases. This occurs because vegetation patches in seaward  
 425 and middle portion of the basin trap the suspended sediment coming from the sea, and  
 426 thus reduce the amount of sediment delivered landwards leading to lower deposition rates,  
 427 which is consistent with the field observation results measured in Jiangsu coast, China  
 428 (Gong et al., 2017). In general, the final equilibrium configuration of the intertidal plat-

429  
430  
431

form exhibits higher elevations near the sea boundary, it decreases progressively landwards for the first 120 m and then it keeps almost constant or slowly decreasing up to the innermost areas.

432  
433  
434  
435  
436  
437

The overall morphological variations of channel cross sections can be characterized through the bankfull cross-sectional width and the maximum cross-sectional depth. The along-channel distribution of these quantities is plotted in Figures 7b,e,h and c,f,i with reference to a representative main channel located in the middle of the tidal basin ( $y = 200 \sim 300$  m). During its development the channel progressively extends from the seaward border to inner areas of the tidal basin, developing mild bends and minor branches.

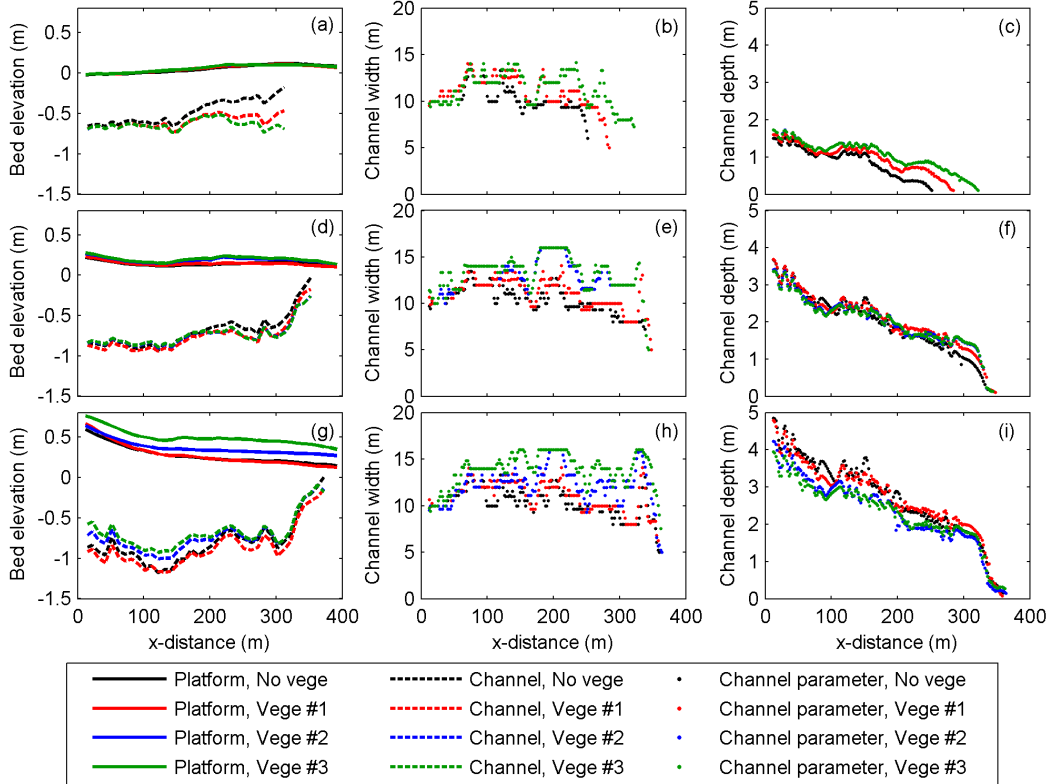


**Figure 7.** The longitudinal distribution of the mean bed elevation in channelized and unchannelized areas (panels a,d,g), along-channel distribution of cross-sectional width (panels b,e,h), and cross-sectional maximum depth (panels c,f,i) are plotted at different times of the morphodynamic evolution: 12 yr, panels a-c; 45 yr, panels d-f; 115 yr, panels g-i. The cross-sectional parameters are measured from a typical channel located in the middle of the tidal basis. Black dots refer to bare soil while red, blue, and green dots denote Vege #1, Vege #2, and Vege #3, respectively.

438  
439  
440  
441

A slight narrowing invariably characterizes the cross-sections close to the seaward boundary, where the adjacent unchanneled areas are dominated by deposition. The cross-sectional width then increases as the channel extends in the central region of the tidal basin. Channel width decreases towards the landward channel head (Figures 7b,e,h).

442  
443  
444  
445

Higher elevations of intertidal areas boosted by vegetation enhance channel widening (blue and green dots in Figures 7e,h). This effect is particularly evident in simulations carried out with Vege #2 and Vege #3. In these two simulations, as compared to Vege #1 and bare soil cases, sediment trapping and organic soil production lead to higher

446 bed elevations of unchanneled areas in the central and landward portions of the basin  
 447 (blue and green continuous lines in Figures 7d,g). Instead, near the seaward border, sim-  
 448 ilar channel widths are attained in all four cases. This is due to the intense settling de-  
 449 position that takes place in this area, which definitely prevails over the contribution of  
 450 vegetation to sediment deposition.

451 Channel depth increases over time approaching an almost equilibrium condition  
 452 as the rate of change in bed elevation tends to vanish. During the first 12 yrs, the chan-  
 453 nel deepens quite rapidly while extending landwards (Figure 7c). After approximately  
 454 45 yr, the channel depth is quite similar for all simulations (Figure 7f). The presence of  
 455 vegetation eventually (after 115 yr) leads to shallower cross sections in both the seaward  
 456 and central areas of the basin (Figure 7i). This effect is particularly evident for Vege #2  
 457 and Vege #3. The higher mean elevation of the adjacent intertidal platform character-  
 458 izing these simulations, as compared to the bare soil case, implies that a smaller volume  
 459 of water needs to be accommodated in channels during the ebb tide. Given also the larger  
 460 cross-sectional width in the case of Vege #2 and #3 (Figure 7h, blue and green dots),  
 461 this reduction in the ebb flow discharge explains why the seaward and central reaches  
 462 of the channel get shallower (Figure 7i).

## 463 4 Discussion

### 464 4.1 Effects of sea level rise

465 In coastal areas, intertidal zones are usually influenced by increasing MSL. Math-  
 466 ematical models provide a fundamental tool to evaluate the possible long-term conse-  
 467 quences of changes in MSL on tidal eco-morphodynamics. In the case of the schematic  
 468 tidal basin considered here, keeping fixed all the parameters listed in Table 1, no ma-  
 469 jor differences are observed for relatively low rates of RSLR (2 mm/yr). Conversely, un-  
 470 der a fairly large rate of RSLR (8 mm/yr), platform elevations fall below MSL, thus cre-  
 471 ating unsuitable conditions for vegetation growth.

472 In the following, we discuss the eco-morphodynamic changes experienced by the  
 473 investigated tidal basin when subject to a RSLR of 4 mm/yr, close to the value of 3.5 mm/yr  
 474 usually adopted for the Venice Lagoon in long-term simulations (e.g. Marani et al., 2007).  
 475 In general, high rates of RSLR and low sediment supplies threaten the development and  
 476 maintenance of salt marshes. For a given sediment supply, as the rate of RSLR increases,  
 477 marsh elevation decreases to increase the deposition rate due to the longer hydroperiod,  
 478 larger water depth and advective transport from the sediment source. However, when  
 479 marsh elevation falls below a given threshold, vegetation cannot survive and the marsh  
 480 platform experiences a transition to a tidal flat (Marani et al., 2007; Kirwan & Temmer-  
 481 man, 2009; Kirwan et al., 2010; D’Alpaos et al., 2011). Furthermore, for a given ampli-  
 482 tude of the tidal wave, higher mean water depths imply weaker shear stresses and thus  
 483 smaller erosion rate and longer deposition period. If sediment supply is large enough,  
 484 bed accretion due to a long-lasting net deposition may keep pace with RSLR, benefit-  
 485 ing from the longer hydro-period induced by the rising sea level. On the contrary, a scarce  
 486 sediment input implies a weaker net deposition, leading to a bed accretion smaller than  
 487 RSLR (D’Alpaos et al., 2011). Clearly, the spatial distribution of sediment concentra-  
 488 tion is in general influenced by the basin topography and the related flow patterns. Then,  
 489 even for a sufficient external sediment supply, different areas within the basin may ex-  
 490 hibit contrasting morphological trends in response to RSLR (van der Wegen, 2013; van  
 491 Maanen et al., 2013). When the sediment input is assumed constant throughout the basin  
 492 as in some idealized modeling frameworks (e.g. D’Alpaos et al., 2006; Sgarabotto et al.,  
 493 2021), the differences in the intertidal platform topography are smoothed out and thus  
 494 these complex evolutionary behaviours cannot be reproduced.

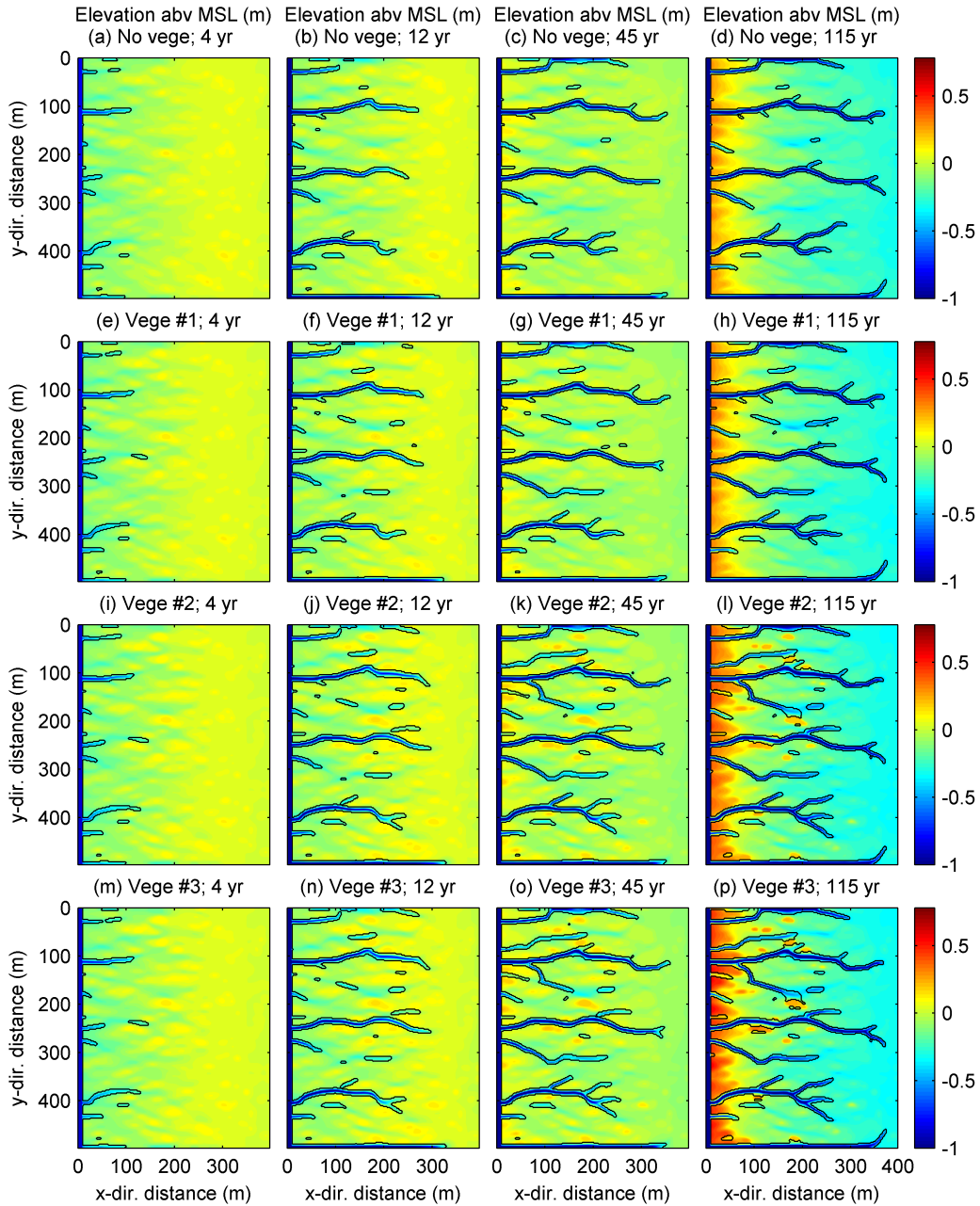


**Figure 8.** The spatial distribution of bed elevation (m), referred to MSL, is plotted at different evolution stages (4, 12, 45, and 115 yr) for a sea level rise of 4 mm/yr. The four simulated cases, are the same of Figure 4: bare soil, panels a-d; Vege #1, panels e-h; Vege #2, panels i-l; Vege #3, panels m-p. Black lines denote the edge of tidal channels.

495 Similarly to simulations carried out in the absence of RSLR, tidal channels start  
 496 to grow from the seaward boundary of the tidal basin and then extend landward through  
 497 headward erosion. After channel formation, the mean basin elevation gradually increases  
 498 due to a positive net deposition rate. Vege #2 and Vege #3 patches start to grow through-  
 499 out the entire basin from the very beginning of the evolution (Figures 8i-l,m-p), while  
 500 Vege #1 needs higher elevations and, hence, begins to encroach the intertidal platform

501 later (Figures 8e-h). However, RSLR dramatically restricts vegetation growth in the  
 502 inner areas of the tidal basin as compared with constant MSL simulations. Indeed, because  
 503 of the progressive landward decay of the transported sediment, these areas hardly keep  
 504 pace with the rate of RSLR and become less prone to vegetation growth. Only some veg-  
 505 etation patches with significant biomass survive because of the locally enhanced bed ac-  
 506 cretion induced by sediment trapping and organic soil production. Outside of these patches,  
 507 bed accretion is definitely lower and leads to a longer hydroperiod, threatening vegeta-  
 508 tion survival. Highly vegetated patches thus hardly extend and become increasingly iso-  
 509 lated. This uneven spatial distribution of vegetation exacerbates the differences in to-  
 510 pography across the tidal basin. Eventually, vegetation biomass inevitably concentrates  
 511 near the seaward border, where higher bed elevations are attained. The basin thus de-  
 512 velops a remarkable landward-decreasing bed slope (Figures 8d,h,l,p).

513 The overall effects of RSLR on tidal-channel and marsh morphology are shown in  
 514 Figure 9 in terms of total channel length and total biomass. In the unvegetated case, the  
 515 increasing mean sea level has little influence on the development of the tidal channel net-  
 516 works, at least for the present schematic basin. As compared with the case with no RSLR  
 517 (Figure 6a), the total channel length measured at the end of the simulation increases slightly,  
 518 by about 2.1%.

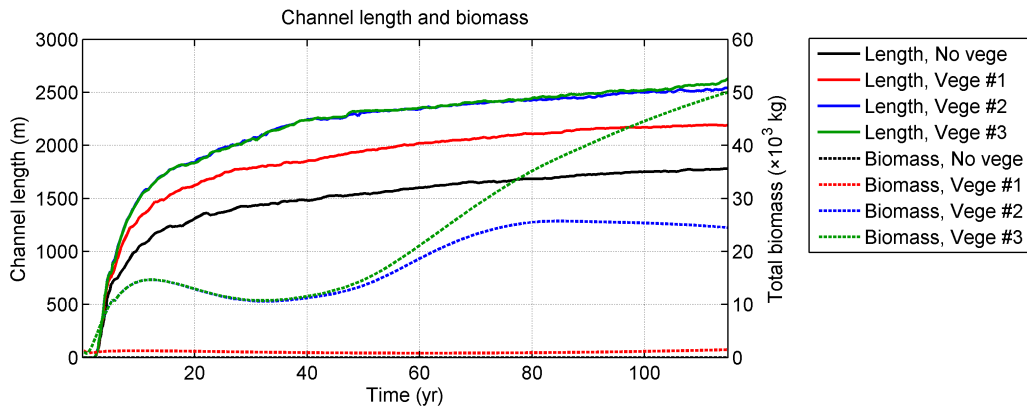


**Figure 9.** Variations in total channel length (continuous lines) and total biomass (dotted lines) are plotted versus time for the various cases considered in the simulations carried out with a sea level rise of 4 mm/yr. Black lines denote the bare soil case; red, blue, and green lines denote Vege #1, Vege #2 and Vege #3 cases, respectively.

519 On the contrary, RSLR has a strong impact on total vegetation growth. Indeed,  
 520 owing to the overall lower relative bed elevation, vegetation biomass is remarkably smaller  
 521 than in simulations carried out with a constant MSL (Figure 6f). As a result, vegeta-  
 522 tion affects the development of tidal channels to a less extent. The total biomass of Vege  
 523 #1 is an order of magnitude smaller than that of Vege #2 and Vege #3. Vegetation growth  
 524 concentrates near the seaward border of the basin where, as shown in Figure 8h, higher  
 525 bed elevations ultimately occur. The total channel length is about 4% shorter than that  
 526 observed in the case of a constant MSL.

527 Also for the other two vegetation types, RSLR causes a remarkable decrease of total  
 528 biomass, which at the end of the simulations turns out to be approximately six times  
 529 (Vege #2) and four times (Vege #3) smaller than in the case of a constant MSL (Fig-  
 530 ure 6f, blue and green lines). Total biomass reduction is particularly severe in the pe-  
 531 riod between 14 and 34 yr when vegetation patches, initially grown in the inner portions

532 of the tidal basin, progressively decrease in size owing to the reduced accretion rate of  
 533 the intertidal platform. In both cases, similarly to Vege #1, biomass eventually concen-  
 534 trates near the seaward basin border. As compared to the bare soil situation, the influ-  
 535 ence of Vege #2 and Vege #3 on the tidal channel morphology is fairly similar and prompts  
 536 a slight increase (about 43 %) in the total channel length.

## 537 4.2 Comparison with field data

538 Multiple environmental factors influence the development of tidal channel networks,  
 539 leading to a wide range of structures and patterns. In the absence of detailed informa-  
 540 tion on the boundary conditions and on the past changes in landforming processes oc-  
 541 curred within an intertidal environment, it is almost impossible to reproduce numeri-  
 542 cally the actual morphology of a tidal channel system. A general comparison between  
 543 the features of real and synthetic channel patterns may however be based on some rel-  
 544 evant statistics (e.g. the mean channel width and length, and the mean channel spac-  
 545 ing).

546 As previously stated, in the present contribution we focus on small tidal environ-  
 547 ments connecting with large channels as those shown in Figure 1, concerning the south  
 548 edge of Warbah Island (Shatt el-Arab Estuary, Kuwait), the Great Ouse River (The Wash,  
 549 UK), the Petaluma River (California, USA), and the Dell’Ancora Channel (Venice La-  
 550 goon, IT). Note that, while Warbah Island is characterized by channels cutting through  
 551 bare tidal flats, the other three cases instead refer to salt-marsh channels.

552 In particular, we applied the model to mimic the features of tidal channels form-  
 553 ing in the rectangular areas depicted with red lines in Figures 1a,b. The tidal basin con-  
 554 sidered in Warbah Island (hereafter denoted with WI) has a length of 600 m and a width  
 555 of 500 m. In Kuwait Bay, the tides are semidiurnal and the tidal range changes from 4.2 m  
 556 (during spring tides) to 0.5 m (during neap tides) (Baby, 2011). Considering the cosine  
 557 tide wave used in the simulation, the tidal range is set to 2 m. Given the lack of specific  
 558 information, the seaward sediment concentration is tentatively set to  $10 \text{ g/m}^3$ , correspond-  
 559 ing to the lower SSC values observed in the northwest Persian Gulf (Al-Ghadban, 2004;  
 560 Al-Yamani et al., 2004). In the case of the salt marsh flanking the Dell’Ancora channel  
 561 in the Venice lagoon (hereafter denoted as VE), the tidal basin length is 80 m and the  
 562 width is 50 m. Similar to other studies carried out for the Venice Lagoon (D’Alpaos &  
 563 Marani, 2016), the tidal forcing is taken to be sinusoidal with amplitude of 0.5 m. The  
 564 input sediment concentration is set to  $3 \text{ g/m}^3$ , and kept constant in time. This value has  
 565 been taken lower than the sediment concentration measured in the neighboring area (about  
 566  $8.6 \text{ g/m}^3$ , Carniello et al., 2012; Venier et al., 2014) to account for the intermittency of  
 567 the wind-events leading to the observed concentration value. Two vegetation scenarios  
 568 are considered. Typically, salt marshes in the Venice Lagoon are colonized by multiple  
 569 species vegetation (Silvestri et al., 2005; D’Alpaos et al., 2007). Vegetation biomass then  
 570 attains high values even when bed elevation reaches relatively high levels. Here, for sen-  
 571 sitivity analysis purposes, two different biomass functions (Vege #VE1 and Vege #VE2)  
 572 have been considered to mimic a multiple species vegetation (Figure 10d). In both cases,  
 573 the biomass is kept fixed after its maximum is attained for a prescribed elevation (0.4 m  
 574 above MSL for Vege #VE1, and 0.1 m above MSL for Vege #VE2). Simulations lasted  
 575 115 yr, such that the channels and the surrounding intertidal platform have approximately  
 576 reached a stable configuration characterized by a vanishing small rate of morphological  
 577 changes.

578 Figures 10a-c show the bed topographies at the end of the simulations. Almost par-  
 579 allel channels grow within the simulated basins, as observed in the field (Figures 10e,f).  
 580 However, compared with the actual channels the numerically generated channels have  
 581 fewer branches. This finding is possibly related to the grid size (2 m for simulation WI

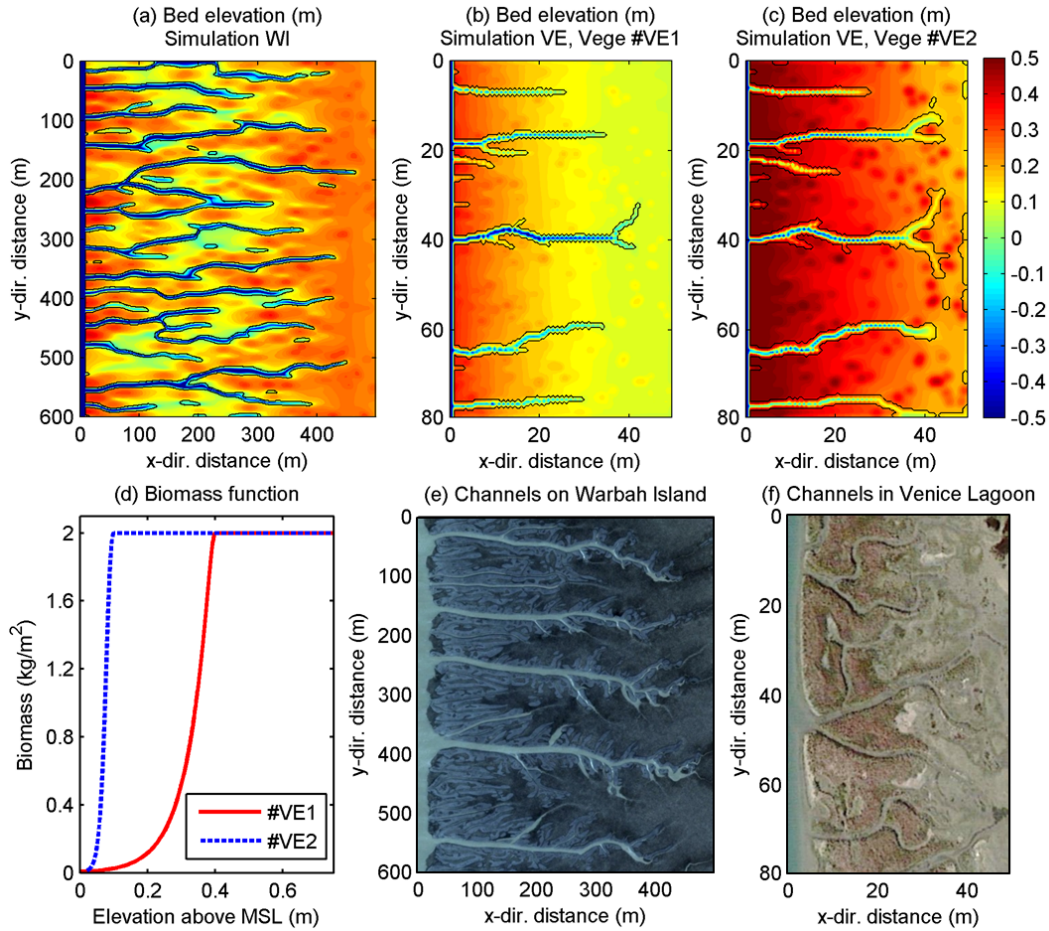


**Figure 10.** The bed topography (expressed in m) obtained after 115 yr in the simulations carried out for a) Warbah Island and b,c) a typical small salt marsh in the Venice lagoon. In this latter case, two different type of vegetation have been considered, Vege #VE1 and Vege #VE2, with biomass functions shown in plot d). (e-f) Enlarged view of the actual channel morphologies observed in WI and VE.

582 and 0.5 m for simulations VE) and the initial bed perturbations used in the simulations,  
 583 which limit the formation of smaller branches.

584 In the case of the VE marsh, the mean length, mean width and mean spacing (both  
 585 measured at the seaward border) of simulated channels are definitely similar to the ac-  
 586 tual ones (Figure 11). Channel features strongly depend on the size of the tidal basin.  
 587 Indeed, the Venice channels investigated here are definitely narrower than synthetic chan-  
 588 nels recently reproduced in Sgarabotto et al. (2021) where mean channel width reaches  
 589 20 m in a basin 100 times larger than that here considered. In the case of WI, simulated  
 590 channels are generally wider and have a larger spacing as compared to channels observed  
 591 in the field. Note that in the simulations the channel length is likely related to the im-  
 592 posed basin length, which exerts some control on the volume of water to be drained dur-  
 593 ing every ebb tide.

594 Clearly, various uncertainties affect the parameters used in the simulations, espe-  
 595 cially for WI (e.g. the externally imposed concentration, the critical shear stresses for  
 596 erosion, initial bed perturbations). These uncertainties might in part explain why the

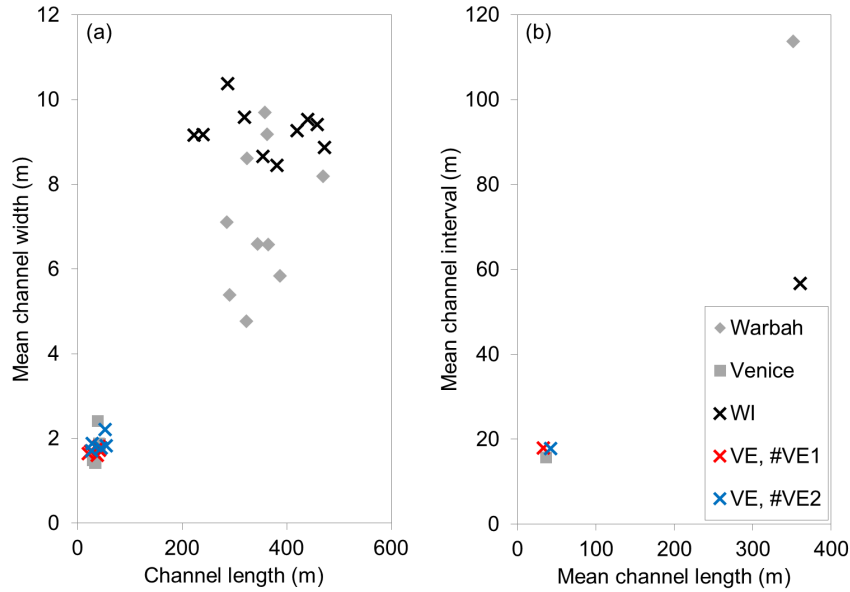


**Figure 11.** a) Mean channel width and b) mean channel interaxis are plotted versus mean channel length for observed and numerically generated tidal channels shown in Figure 10.

597 simulated WI channels exhibit a smaller range of width values as compared to reality.  
 598 Certainly, the simulated environmental conditions are simpler and more homogeneous  
 599 than in the field. Besides, near bank flow, and hence bank erosion, are poorly represented  
 600 in the model. The initial bed topography can also affect the channel network morphol-  
 601 ogy. The initial randomly generated disturbances superposed to an otherwise horizon-  
 602 tal bed may influence the final channel network geometry, leading in the case of WI to  
 603 less spaced channels than in the field.

### 604 4.3 Model limitations

605 The present modeling framework is based on some relevant assumptions. First, fric-  
 606 tion is assumed to dominate over inertia (Rinaldo et al., 1999) in the momentum equa-  
 607 tions. Nevertheless, inertia can play an important role within the channels as well as near  
 608 vegetation patches, leading to longer wakes behind them (Van Oyen et al., 2014). Sec-  
 609 ond, erosion at the channel banks and at the seaward border of the tidal basin is described  
 610 approximately as a continuous process. No sub-grid parameterization is used to account  
 611 for the actual shape of the bank/border and of localized and intermittent bank collapse  
 612 events. These approximations have surely an influence on channel width computations.  
 613 Then the condition (25) imposed at the seaward boundary to limit the Froude number  
 614 during late ebb and early flood may have some influence on the morphology eventually  
 615 attained by the seaward border of the tidal basin. Wave-induced erosion, not accounted  
 616 for in the model, may also matter even in the presence of a vegetated platform (e.g. Marani  
 617 et al., 2011; Mariotti & Fagherazzi, 2013; Leonardi & Fagherazzi, 2014; Leonardi et al.,  
 618 2016). Finally, the offline technique for the bed update may affect the synthetic mor-  
 619 phologies. Overall, despite the simplifications introduced with respect to 2-D morpho-  
 620 dynamic models (Hibma et al., 2003; Van der Wegen & Roelvink, 2008; Coco et al., 2013;  
 621 Boelens et al., 2018), the present model is deemed to reproduce correctly the eco-morphodynamic  
 622 evolution of the various morphological units composing small tidal basins, producing tidal  
 623 morphologies which reasonably resemble those observed in the field.



## 5 Conclusions

This study focused on the eco-morphodynamic co-evolution of tidal channels and salt marshes in a schematic basin, mimicking tidal environments flanking large tidal channels or tidal rivers. The co-evolution is simulated through a bio-morphodynamic model which accounts for wetting-and-drying processes and vegetation-induced roughness. Different types of vegetation have been considered, each characterized by a specific biomass function depending on bed elevation. Simulations have been carried out by letting the system evolve starting from a horizontal, slightly and randomly-perturbed bed, under the influence of a forcing tide and a sediment concentration imposed at the seaward boundary. The main results of our analysis can be summarized as follows.

Model results successfully mimic the morphologies observed in the field for both bare soil and vegetated conditions. In general, widely spread vegetation patches are found to definitely affect the structure of the tidal channel network. The increased friction produced by vegetation feeds back on the flow field and, consequently, on the erosion and deposition patterns that ultimately determine the structure of the tidal channel network.

Vegetation with an optimal elevation for biomass production close to MSL is found to strongly promote the development of tidal channels as compared with the bare soil case. Specifically, channels extend more rapidly landward, through headward erosion. Their cross sections are usually wider and shallower. In addition, more channel branches grow, forming more complex network structures with a higher drainage efficiency with respect to the bare soil case, as well as to the case of vegetation with a higher optimal elevation for biomass production.

In general, vegetation starts to colonize the intertidal platform from the seaward border, where the externally supplied sediment concentration ensures a more rapid bed accretion. Vegetation then extends landwards. The presence of pioneer vegetation (mimicked by introducing randomly distributed perturbations of the initial bed topography) enhances the deposition on unchanneled areas, leading to faster growth of salt marshes, especially for species with optimal biomass production occurring closer to MSL. Vegetation trapping of suspended sediment in the seaward and middle portions of the tidal basin invariably reduces the amount of sediment delivered to landward areas, weakening the sedimentation there.

In the presence of RSLR, owing to the lower relative bed elevation above MSL, vegetation growth is limited and, consequently, its control on channel morphology is reduced. Given a sufficient seaward sediment supply, the deposition rate at the seaward border of the basin can keep pace with the rate of RSLR. Conversely, the inner basin becomes incrementally submerged and a landward bed slope forms. Vegetation patches with high biomass become increasingly isolated. Indeed, the bare tidal platform adjacent to these patches experiences a deposition rate much lower than that needed to counteract the effect of RSLR.

The simulated channel networks exhibit a reasonable similarity with the parallel channel patterns observed in tidal areas adjacent to larger tidal channels. Nevertheless, the simulated cross sections are somewhat wider than those observed in the field, especially the smaller channel branches. This finding is strictly related to the relatively large grid size used in the simulations, which prevents reproducing correctly the smaller creek geometry. Clearly, the lack of a sub-grid parametrization of bank erosion and bank collapse events can also explain the differences between simulated and real channel geometries.

## Data Availability Statement

The data used in the current study are available at <https://doi.org/10.5281/zenodo.5075102>.

## Acknowledgments

This research was supported by the University of Padova, by the ICEA department within the University of Padova and by National Natural Science Foundation of China (51620105005 and 51879095). Liang Geng acknowledges the China Scholarship Council (CSC) for the support of doctoral study. We would like to express our very great appreciation to Prof. Tomas Van Oyen from Ghent University and Prof. Mario Putti from the University of Padova for their support and suggestions on this model.

## References

- Al-Ghadban, A. N. (2004). Assessment of suspended sediment in Kuwait Bay using Landsat and SPOT images. *Kuwait Journal of Science and Engineering*, 31(2), 155–172.
- Allen, J. R. (2000). Morphodynamics of holocene salt marshes: A review sketch from the Atlantic and Southern North Sea coasts of Europe. *Quaternary Science Reviews*, 19(12), 1155–1231.
- Al-Yamani, F. Y., Bishop, J., Ramadhan, E., Al-Husaini, M., & Al-Ghadban, A. N. (2004). *Oceanographic atlas of Kuwait's waters*. Kuwait: Kuwait Institute for Scientific Research.
- Baby, S. (2011). Information research on coastal morphological environment of Kuwait, organizations, role and coastal legislations. *Emirates Journal for Engineering Research*, 16(2), 7–24.
- Balke, T., Bouma, T. J., Horstman, E. M., Webb, E. L., Erftemeijer, P. L., & Herman, P. M. (2011). Windows of opportunity: Thresholds to mangrove seedling establishment on tidal flats. *Marine Ecology Progress Series*, 440, 1–9.
- Balke, T., Herman, P. M., & Bouma, T. J. (2014). Critical transitions in disturbance-driven ecosystems: Identifying Windows of Opportunity for recovery. *Journal of Ecology*, 102(3), 700–708.
- Belliard, J.-P., Toffolon, M., Carniello, L., & D'Alpaos, A. (2015). An ecogeomorphic model of tidal channel initiation and elaboration in progressive marsh accretional contexts. *Journal of Geophysical Research: Earth Surface*, 120(6), 1040–1064.
- Bendoni, M., Mel, R., Solari, L., Lanzoni, S., Francalanci, S., & Oumeraci, H. (2016). Insights into lateral marsh retreat mechanism through localized field measurements. *Water Resources Research*, 52, 1446–1464.
- Boelens, T., Schuttelaars, H., Schramkowski, G., & De Mulder, T. (2018). The effect of geometry and tidal forcing on hydrodynamics and net sediment transport in semi-enclosed tidal basins. *Ocean Dynamics*, 68(10), 1285–1309.
- Bouma, T. J., van Belzen, J., Balke, T., Zhu, Z., Airolidi, L., Blight, A. J., ... Herman, P. M. (2014). Identifying knowledge gaps hampering application of intertidal habitats in coastal protection: Opportunities & steps to take. *Coastal Engineering*, 87, 147–157.
- Carniello, L., Defina, A., & D'Alpaos, L. (2012). Modeling sand-mud transport induced by tidal currents and wind waves in shallow microtidal basins: Application to the Venice Lagoon (Italy). *Estuarine, Coastal and Shelf Science*, 102, 105–115.
- Chen, X., Zhang, C., Paterson, D., Thompson, C., Townend, I., Gong, Z., ... Feng, Q. (2017). Hindered erosion: The biological mediation of noncohesive sediment behavior. *Water Resources Research*, 53(6), 4787–4801.
- Coco, G., Zhou, Z., van Maanen, B., Olabarrieta, M., Tinoco, R., & Townend, I. (2013). Morphodynamics of tidal networks: Advances and challenges. *Marine Geology*, 346, 1–16.
- Cowell, P., & Thom, B. (1994). Morphodynamics of coastal evolution. In R. Carter & C. Woodroffe (Eds.), *Coastal evolution: Late Quaternary shoreline morphodynamics* (pp. 33–86). Cambridge University Press, Cambridge.

- 726 D'Alpaos, A., Lanzoni, S., Marani, M., Fagherazzi, S., & Rinaldo, A. (2005). Tidal  
727 network ontogeny: Channel initiation and early development. *Journal of Geo-*  
728 *physical Research: Earth Surface*, 110(F02001), 1–14.
- 729 D'Alpaos, A., Lanzoni, S., Marani, M., & Rinaldo, A. (2007). Landscape evolu-  
730 tion in tidal embayments: Modeling the interplay of erosion, sedimentation,  
731 and vegetation dynamics. *Journal of Geophysical Research: Earth Surface*,  
732 112(F01008), 1–17.
- 733 D'Alpaos, A., Lanzoni, S., Mudd, S. M., & Fagherazzi, S. (2006). Modeling the in-  
734 fluence of hydroperiod and vegetation on the cross-sectional formation of tidal  
735 channels. *Estuarine, Coastal and Shelf Science*, 69(3-4), 311–324.
- 736 D'Alpaos, A., & Marani, M. (2016). Reading the signatures of biologic–geomorphic  
737 feedbacks in salt-marsh landscapes. *Advances in water resources*, 93, 265–275.
- 738 D'Alpaos, A., Mudd, S. M., & Carniello, L. (2011). Dynamic response of marshes  
739 to perturbations in suspended sediment concentrations and rates of relative sea  
740 level rise. *Journal of Geophysical Research: Earth Surface*, 116(F04020), 1–13.
- 741 Defina, A. (2000). Two-dimensional shallow flow equations for partially dry areas.  
742 *Water resources research*, 36(11), 3251–3264.
- 743 De Swart, H., & Zimmerman, J. (2009). Morphodynamics of tidal inlet systems. *An-*  
744 *ual review of fluid mechanics*, 41, 203–229.
- 745 Fagherazzi, S., Carniello, L., D'Alpaos, L., & Defina, A. (2006). Critical bifurcation  
746 of shallow microtidal landforms in tidal flats and salt marshes. *Proceedings of*  
747 *the National Academy of Sciences*, 103(22), 8337–8341.
- 748 Fagherazzi, S., Gabet, E. J., & Furbish, D. J. (2004). The effect of bidirectional flow  
749 on tidal channel planforms. *Earth Surface Processes and Landforms*, 29(3),  
750 295–309.
- 751 FitzGerald, D. M., & Hughes, Z. (2019). Marsh processes and their response to  
752 climate change and sea-level rise. *Annual Review of Earth and Planetary Sci-*  
753 *ences*, 47, 481–517.
- 754 Friedrichs, C. T., & Perry, J. E. (2001). Tidal salt marsh morphodynamics: A syn-  
755 thesis. *Journal of Coastal Research*, 7–37.
- 756 Geng, L., Gong, Z., Lanzoni, S., & D'Alpaos, A. (2018). A new method for auto-  
757 matic definition of tidal creek networks. *Journal of Coastal Research*(85), 156–  
758 160.
- 759 Gong, Z., Jin, C., Zhang, C., Zhou, Z., Zhang, Q., & Li, H. (2017). Temporal and  
760 spatial morphological variations along a cross-shore intertidal profile, Jiangsu,  
761 China. *Continental Shelf Research*, 144, 1–9.
- 762 Gong, Z., Zhao, K., Zhang, C., Dai, W., Coco, G., & Zhou, Z. (2018). The role of  
763 bank collapse on tidal creek ontogeny: A novel process-based model for bank  
764 retreat. *Geomorphology*, 311, 13–26.
- 765 Hibma, A., Schuttelaars, H. M., & Wang, Z. B. (2003). Comparison of longitudinal  
766 equilibrium profiles of estuaries in idealized and process-based models. *Ocean*  
767 *Dynamics*, 53(3), 252–269.
- 768 Horton, R. E. (1945). Erosional development of streams and their drainage basins;  
769 hydrophysical approach to quantitative morphology. *Geological society of*  
770 *America bulletin*, 56(3), 275–370.
- 771 Hu, Z., van Belzen, J., van Der Wal, D., Balke, T., Wang, Z. B., Stive, M., &  
772 Bouma, T. J. (2015). Windows of opportunity for salt marsh vegetation estab-  
773 lishment on bare tidal flats: The importance of temporal and spatial variability  
774 in hydrodynamic forcing. *Journal of Geophysical Research: Biogeosciences*,  
775 120(7), 1450–1469.
- 776 Hughes, Z. J. (2012). Tidal channels on tidal flats and marshes. In R. A. Davis Jr  
777 & R. W. Dalrymple (Eds.), *Principles of tidal sedimentology* (pp. 269–300).  
778 Springer.
- 779 Kirwan, M. L., Guntenspergen, G. R., D'Alpaos, A., Morris, J. T., Mudd, S. M., &  
780 Temmerman, S. (2010). Limits on the adaptability of coastal marshes to rising

- 781 sea level. *Geophysical research letters*, 37(L23401), 1–5.
- 782 Kirwan, M. L., & Megonigal, J. P. (2013). Tidal wetland stability in the face of hu-  
783 man impacts and sea-level rise. *Nature*, 504(7478), 53–60.
- 784 Kirwan, M. L., & Temmerman, S. (2009). Coastal marsh response to historical  
785 and future sea-level acceleration. *Quaternary Science Reviews*, 28(17–18),  
786 1801–1808.
- 787 Kleinhans, M. G., van Scheltinga, R. T., van Der Vegt, M., & Markies, H. (2015).  
788 Turning the tide: Growth and dynamics of a tidal basin and inlet in experi-  
789 ments. *Journal of Geophysical Research: Earth Surface*, 120(1), 95–119.
- 790 Lawrence, D., Allen, J. R., & Havelock, G. (2004). Salt marsh morphodynamics: An  
791 investigation of tidal flows and marsh channel equilibrium. *Journal of Coastal  
792 Research*, 20(1), 301–316.
- 793 Leonardi, N., & Fagherazzi, S. (2014). How waves shape salt marshes. *Geology*,  
794 42(10), 887–890.
- 795 Leonardi, N., Ganju, N. K., & Fagherazzi, S. (2016). A linear relationship between  
796 wave power and erosion determines salt-marsh resilience to violent storms and  
797 hurricanes. *Proceedings of the National Academy of Sciences*, 113(1), 64–68.
- 798 Li, X., Leonardi, N., & Plater, A. J. (2019). A stochastic approach to modeling  
799 tidal creek evolution: Exploring environmental influences on creek topologies  
800 through ensemble predictions. *Geophysical Research Letters*, 46(23), 13836–  
801 13844.
- 802 Lovelock, C. E., Bennion, V., Grinham, A., & Cahoon, D. R. (2011). The role of  
803 surface and subsurface processes in keeping pace with sea level rise in intertidal  
804 wetlands of Moreton Bay, Queensland, Australia. *Ecosystems*, 14(5), 745–757.
- 805 Marani, M., Belluco, E., D’Alpaos, A., Defina, A., Lanzoni, S., & Rinaldo, A.  
806 (2003). On the drainage density of tidal networks. *Water Resources Research*,  
807 39(2), 1040.
- 808 Marani, M., Da Lio, C., & D’Alpaos, A. (2013). Vegetation engineers marsh mor-  
809 phology through multiple competing stable states. *Proceedings of the National  
810 Academy of Sciences*, 110(9), 3259–3263.
- 811 Marani, M., D’Alpaos, A., Lanzoni, S., Carniello, L., & Rinaldo, A. (2007).  
812 Biologically-controlled multiple equilibria of tidal landforms and the fate of  
813 the Venice Lagoon. *Geophysical Research Letters*, 34(L11402), 1–5.
- 814 Marani, M., D’Alpaos, A., Lanzoni, S., & Santalucia, M. (2011). Understanding  
815 and predicting wave erosion of marsh edges. *Geophysical Research Letters*,  
816 38(L21401), 1–5.
- 817 Marani, M., Lanzoni, S., Zandolin, D., Seminara, G., & Rinaldo, A. (2002). Tidal  
818 meanders. *Water Resources Research*, 38(11), 1–14.
- 819 Mariotti, G. (2018). Marsh channel morphological response to sea level rise and sed-  
820 iment supply. *Estuarine, Coastal and Shelf Science*, 209, 89–101.
- 821 Mariotti, G., & Fagherazzi, S. (2013). Critical width of tidal flats triggers marsh  
822 collapse in the absence of sea-level rise. *Proceedings of the national Academy of  
823 Sciences*, 110(14), 5353–5356.
- 824 Mitsch, W. J., & Gosselink, J. G. (2000). The value of wetlands: Importance of scale  
825 and landscape setting. *Ecological Economics*, 35(1), 25–33.
- 826 Morris, J. T., Sundareshwar, P., Nietch, C. T., Kjerfve, B., & Cahoon, D. R. (2002).  
827 Responses of coastal wetlands to rising sea level. *Ecology*, 83(10), 2869–2877.
- 828 Mudd, S. M., D’Alpaos, A., & Morris, J. T. (2010). How does vegetation affect  
829 sedimentation on tidal marshes? Investigating particle capture and hydrody-  
830 namic controls on biologically mediated sedimentation. *Journal of Geophysical  
831 Research: Earth Surface*, 115(F03029), 1–14.
- 832 Mudd, S. M., Fagherazzi, S., Morris, J. T., & Furbish, D. J. (2004). Flow, sedimen-  
833 tation, and biomass production on a vegetated salt marsh in South Carolina:  
834 Toward a predictive model of marsh morphologic and ecologic evolution. In  
835 S. Fagherazzi, A. Marani, & L. Blum (Eds.), *The ecogeomorphology of tidal*

- marshes, *coastal estuarine stud* (Vol. 59, pp. 165–187). AGU, Washington, D. C.
- Palmer, M. R., Nepf, H. M., Pettersson, T. J., & Ackerman, J. D. (2004). Observations of particle capture on a cylindrical collector: Implications for particle accumulation and removal in aquatic systems. *Limnology and Oceanography*, *49*(1), 76–85.
- Pilkey, O. H., & Cooper, J. A. G. (2004). Society and sea level rise. *Science*, *303*(5665), 1781–1782.
- Rinaldo, A., Fagherazzi, S., Lanzoni, S., Marani, M., & Dietrich, W. E. (1999). Tidal networks: 2. Watershed delineation and comparative network morphology. *Water Resources Research*, *35*(12), 3905–3917.
- Roelvink, J. (2006). Coastal morphodynamic evolution techniques. *Coastal engineering*, *53*(2-3), 277–287.
- Sgarabotto, A., D’Alpaos, A., & Lanzoni, S. (2021). Effects of vegetation, sediment supply and sea level rise on the morphodynamic evolution of tidal channels. *Water Resources Research*(e2020WR028577), 1–24.
- Silvestri, S., Defina, A., & Marani, M. (2005). Tidal regime, salinity and salt marsh plant zonation. *Estuarine, coastal and shelf science*, *62*(1-2), 119–130.
- Stefanon, L., Carniello, L., D’Alpaos, A., & Rinaldo, A. (2012). Signatures of sea level changes on tidal geomorphology: Experiments on network incision and retreat. *Geophysical Research Letters*, *39*(L12402), 1–6.
- Temmerman, S., Bouma, T., van de Koppel, J., van der Wal, D., De Vries, M., & Herman, P. (2007). Vegetation causes channel erosion in a tidal landscape. *Geology*, *35*(7), 631–634.
- Temmerman, S., Bouma, T. J., Govers, G., Wang, Z. B., De Vries, M., & Herman, P. (2005). Impact of vegetation on flow routing and sedimentation patterns: Three-dimensional modeling for a tidal marsh. *Journal of Geophysical Research: Earth Surface*, *110*(F04019), 1–18.
- Temmerman, S., Moonen, P., Schoelynck, J., Govers, G., & Bouma, T. J. (2012). Impact of vegetation die-off on spatial flow patterns over a tidal marsh. *Geophysical Research Letters*, *39*(L03406), 1–5.
- Toffolon, M., & Lanzoni, S. (2010). Morphological equilibrium of short channels dissecting the tidal flats of coastal lagoons. *Journal of Geophysical Research: Earth Surface*, *115*(F04036), 1–15.
- Tommasini, L., Carniello, L., Ghinassi, M., Roner, M., & D’Alpaos, A. (2019). Changes in the wind-wave field and related salt-marsh lateral erosion: Inferences from the evolution of the Venice Lagoon in the last four centuries. *Earth Surface Processes and Landforms*, *44*(8), 1633–1646.
- Toy, T. J., Foster, G. R., & Renard, K. G. (2002). *Soil erosion: Processes, prediction, measurement, and control*. New York: John Wiley & Sons.
- Vandenbruwaene, W., Meire, P., & Temmerman, S. (2012). Formation and evolution of a tidal channel network within a constructed tidal marsh. *Geomorphology*, *151*, 114–125.
- Vandenbruwaene, W., Temmerman, S., Bouma, T., Klaassen, P., De Vries, M., Callaghan, D., ... Meire, P. (2011). Flow interaction with dynamic vegetation patches: Implications for biogeomorphic evolution of a tidal landscape. *Journal of Geophysical Research: Earth Surface*, *116*(F01008), 1–13.
- van der Wegen, M. (2013). Numerical modeling of the impact of sea level rise on tidal basin morphodynamics. *Journal of Geophysical Research: Earth Surface*, *118*(2), 447–460.
- van der Wegen, M., Dastgheib, A., & Roelvink, J. (2010). Morphodynamic modeling of tidal channel evolution in comparison to empirical P-A relationship. *Coastal Engineering*, *57*(9), 827–837.
- van der Wegen, M., & Roelvink, J. (2008). Long-term morphodynamic evolution of a tidal embayment using a two-dimensional, process-based model. *Journal of*

- 891 *Geophysical Research: Oceans*, 113(C03016), 1–23.
- 892 van Maanen, B., Coco, G., Bryan, K. R., & Friedrichs, C. T. (2013). Modeling the  
893 morphodynamic response of tidal embayments to sea-level rise. *Ocean Dynam-*  
894 *ics*, 63(11-12), 1249–1262.
- 895 van Oyen, T., Carniello, L., D’Alpaos, A., Temmerman, S., Troch, P., & Lanzoni,  
896 S. (2014). An approximate solution to the flow field on vegetated intertidal  
897 platforms: Applicability and limitations. *Journal of Geophysical Research:*  
898 *Earth Surface*, 119(8), 1682–1703.
- 899 Venier, C., D’Alpaos, A., & Marani, M. (2014). Evaluation of sediment properties  
900 using wind and turbidity observations in the shallow tidal areas of the Venice  
901 Lagoon. *Journal of Geophysical Research: Earth Surface*, 119(7), 1604–1616.
- 902 Wright, L., & Thom, B. (1977). Coastal depositional landforms: A morphodynamic  
903 approach. *Progress in Physical Geography*, 1(3), 412–459.
- 904 Yallop, M. C., de Winder, B., Paterson, D. M., & Stal, L. J. (1994). Comparative  
905 structure, primary production and biogenic stabilisation of cohesive and non-  
906 cohesive marine sediments inhabited by microphytobenthos. *Estuarine Coastal*  
907 *Shelf Sciences*, 39, 565–582.
- 908 Zedler, J. B., & Kercher, S. (2005). Wetland resources: Status, trends, ecosystem  
909 services, and restorability. *Annu. Rev. Environ. Resour.*, 30, 39–74.
- 910 Zhao, K., Gong, Z., Xu, F., Zhou, Z., Zhang, C., Perillo, G. M. E., & Coco, G.  
911 (2019). The role of collapsed bank soil on tidal channel evolution: A process-  
912 based model involving bank collapse and sediment dynamics. *Water Resources*  
913 *Research*, 55(11), 9051–9071.
- 914 Zhou, Z., Stefanon, L., Olabarrieta, M., D’Alpaos, A., Carniello, L., & Coco, G.  
915 (2014). Analysis of the drainage density of experimental and modelled tidal  
916 networks. *Earth Surface Dynamics*, 2(1), 105–116.
- 917 Zhou, Z., Ye, Q., & Coco, G. (2016). A one-dimensional biomorphodynamic model  
918 of tidal flats: Sediment sorting, marsh distribution, and carbon accumulation  
919 under sea level rise. *Advances in Water Resources*, 93, 288–302.